Accurate Electronic and Optical Properties of Organic Doublet Radicals Using Machine Learned Range-Separated Functionals

Cheng-Wei Ju,[†,‡] Yili Shen,[¶,§] Ethan J. French,[†,‖,⊥] Jun Yi,[†,#] Hongshan Bi,[†] Aaron Tian,[¶,‖] and Zhou Lin*[,†]

†*Department of Chemistry, University of Massachusetts, Amherst, MA 01003, United States*

‡*Pritzker School of Molecular Engineering, The University of Chicago, Chicago, IL, 60637, United States*

¶*Manning College of Information and Computer Sciences, University of Massachusetts, Amherst, MA 01003, United States*

§*Department of Computer Science and Engineering, University of Notre Dame, Notre Dame, IN 46556*

‖*Department of Mathematics and Statistics, University of Massachusetts, Amherst, MA 01003, United States*

⊥*Athinoula A. Martinos Center for Biomedical Imaging, Department of Radiology, Massachusetts General Hospital and Harvard Medical School, Charlestown, MA 02129, United States*

#*Department of Chemistry, Wake Forest University, Winston-Salem, NC 27109, United States*

E-mail: zhoulin@umass.edu

Abstract

Luminescent organic semiconducting doublet-spin radicals are unique and emergent optical materials because their fluorescent quantum yields (Φ_{fl}) are not compromised by the spin-flipping intersystem crossing (ISC) into a dark high-spin state. The multi-configurational nature of these radicals challenges their electronic structure calculations in the framework of single-reference density functional theory (DFT) and introduces room for method improvement. In the present study, we extended our earlier development of ML-ωPBE [*J. Phys. Chem. Lett.*, 2021, 12, 9516], a range-separated hybrid (RSH) exchange–correlation (XC) functional constructed using the *stacked ensemble machine learning* (SEML) algorithm, from closed-shell organic semiconducting molecules to doublet-spin organic semiconducting radicals. We assessed its performance for a new test set of 64 doublet-spin radicals from five categories while placing all previously compiled 3,926 closed-shell molecules in the new training set. Interestingly, ML-ωPBE agrees with the first-principles OT-ωPBE functional regarding the prediction of the molecule-dependent range-separation parameter (ω), with a small mean absolute error (MAE) of 0.0197 a_0^{-1} but saves the computational cost by 2.46 orders of magnitude. This result demonstrates an outstanding *domain adaptation* capacity of ML-ωPBE for diverse organic semiconducting species. To further assess the predictive power of ML-ωPBE in experimental observables, we also applied it to evaluate absorption and fluorescence energies (E_{abs} and E_{fl}), using linear-response time-dependent DFT (TDDFT) and compared its behavior with nine popular XC functionals. For most radicals, ML-ωPBE reproduces experimental measurements of E_{abs} and E_{fl} with small MAEs of 0.299 and 0.254 eV, only marginally different from OT-ωPBE. Our work illustrates a successful extension of the SEML framework from closed-shell molecules to doublet-spin radicals and will open the venue for calculating optical properties for organic semiconductors using single-reference TDDFT.

Introduction

An organic semiconducting doublet-spin radical can stabilize its unpaired electron through the delocalized π-conjugation and exhibit a non-conventional *non-Aufbau* configuration where the singly occupied molecular orbital (SOMO) is lower-lying than the highest (doubly) occupied molecular orbital (HOMO).[1–10] Such a long-lived open-shell configuration and the resulting compelling physicochemical characteristics, especially controllable optical properties between the doublet ground (D_0) and excited states ($D_{n\geq 1}$), make a radical like this a promising functional material for emergent scientific fields. For example, in photothermal therapy (PTT), a radical anion like a supramolecular complex of benzodithiophene-fused perylene diimide (BPDI) and cucurbit[7]uril (CB[7]) absorbs biologically transparent near-infrared (NIR) light and dissipates the photon energy as heat.[11–15] In an organic light-emitting diode (OLED), the D_1 state can, in principle, reach a 100% fluorescent quantum yield (Φ_{fl}) because it does not favor the intersystem crossing (ISC) into a high-spin dark state.[4,7,16–18]

The open-shell character of such an organic semiconducting radical makes its ground and excited state electronic structures challenging to calculate.[19] Density functional theory (DFT) based multiconfigurational approaches can be physically correct and reliable for this purpose, including complete-active-space density functional theory (CAS-DFT),[20–22] multiconfiguration pair DFT (MC-PDFT),[23–25] multiconfigurational short-range density-functional theory (MC-srDFT),[26–28] and multistate density functional theory (MSDFT).[29–31] However, applications of these multiconfigurational DFT approaches have been limited to small and simple systems because they are less user-friendly in terms of the difficult construction of an appropriate active space without prior knowledge of the electronic structure and the expensive computational cost ($\simeq N_{\mathrm{act}}N_{\mathrm{orb}}^4$) for an organic semiconductor species with a typical size.[32–34]

The low computational cost ($\simeq N_{\mathrm{orb}}^3$) and the black-box character of regular single-reference DFT and linear-response time-dependent DFT (TDDFT) make themselves appealing again for organic semiconducting radicals despite the above-mentioned theoretical

challenges and insufficient reliable benchmarks. DFT and TDDFT can generate ground and/or excited state electronic structures of these radicals to a desired accuracy after careful development and calibration of the exchange–correlation (XC) functional.[35–44] Head-Gordon and coworkers performed systematic studies for excited state properties of polycyclic aromatic hydrocarbon (PAH) radical ions[37,45–49] using original TDDFT and its simplified variant with the Tamm–Dancoff approximation (TDA)[50] along with common functionals like BLYP[51,52] and B3LYP.[51–53] They found that TDDFT and TDDFT/TDA both reproduced experimental excited state energies with errors smaller than 0.3 eV when the basis set was reasonably large, despite inexact XC functionals and adiabatic approximations and the inability to treat double excitations in a single-reference framework.[54,55] They also concluded that TDDFT/TDA outperformed TDDFT in capturing correct states by overcoming the orbital instability problem existing for some radicals.[50,56–60] They further assigned the strongest absorption of each radical to involve its SOMO.

Other researchers, such as Joblin,[38,61–63] Jacquemin,[40] Grimme,[64,65] Furche,[66–68] and Allouche,[69] performed similar benchmark analyses on organic semiconducting radicals using DFT and TDDFT and obtained essential insights into their electronic structures. All these DFT-based studies demonstrated the advantage of using a global hybrid functional (GH)[53,70–72] or a range-separated hybrid (RSH) functional[73–84] with molecule-dependent parameters for organic semiconducting radicals. This is due to the necessity to balance the accuracy of the electronic density between the Hartree–Fock (HF) exchange functional and a (semi)local XC functional like local-density approximation (LDA),[77,85] Becke88 exchange with "one-parameter progressive" correlation (BOP),[86,87] or Perdew–Burke–Ernzerhof (PBE).[88–90]

One outstanding example of a molecule-dependent RSH functional was developed by Kronik, Baer, and their coworkers based on the idea of optimal tuning (OT) based on Koopmans' theorem.[91–97] They utilized the range-separation parameter (ω), which characterizes the inverse distance at which the functional transitions from a (semi-)local formula in the short range to the HF formula in the long range, appearing in the separation of the Coulomb

operator

$$\frac{1}{|\mathbf{r}-\mathbf{r}'|} = \underbrace{\frac{1-\mathrm{erf}(\omega|\mathbf{r}-\mathbf{r}'|)}{|\mathbf{r}-\mathbf{r}'|}}_{\text{short range}} + \underbrace{\frac{\mathrm{erf}(\omega|\mathbf{r}-\mathbf{r}'|)}{|\mathbf{r}-\mathbf{r}'|}}_{\text{long range}} \tag{1}$$

They optimized the value of ω by minimizing the metrics of

$$J^2(\omega) = [\varepsilon_{\mathrm{HOMO}}(\omega) + I(\omega)]^2 + [\varepsilon_{\mathrm{LUMO}}(\omega) + A(\omega)]^2 \tag{2}$$

However, this non-empirical, first-principles OT protocol is expensive for large organic semiconducting compounds because it can cost twenty or more converged SCF calculations to determine a single value of ω without implementing the analytical gradient. In our previous study, we spent an average of 41,940 seconds of CPU time to optimally tune ω for each molecule in our training set.[84]

Motivated by the urgent demand to efficiently determine the molecule-dependent value of ω, as well as the rapid advancement in state-of-the-art machine learning (ML) models, we designed a new RSH functional referred to as ML-ωPBE.[84] Just like OT-ωPBE, we utilized the same XC formula as LC-ωPBE with an arbitrary value of ω and optimized the value of ω based on a *stacked ensemble machine learning* (SEML) algorithm[98–103] and a *composite molecular descriptor* (CMD).[104–109] We systematically trained and benchmarked ML-ωPBE using 3,926 closed-shell organic semiconducting molecules.[84,110–115] The value of ω generated by well-trained ML-ωPBE (ω_{ML}) agreed perfectly with its counterpart from OT-ωPBE (ω_{OT}). The mean absolute error (MAE) was as small as 2.5% of the average ω_{OT} ($\langle\omega_{\mathrm{OT}}\rangle$), but the computational cost was as low as 0.22%. We also compared ML-ωPBE-predicted optical properties with OT-ωPBE and many popular functionals,[51–53,70–72,74,79,88,89,116] and found that ML-ωPBE reproduced the accuracy of OT-ωPBE and outperformed everyone else. It is worth noticing that the test set in that study included some "external" molecules with *no* structural analogs present in the training set.[83,117–119] Successful predictions for these external molecules indicate the advantages of our SEML model and ML-ωPBE functional that were

seldom observed in other ML models and XC functionals, referred to as a substantial capacity in transferability or *domain adaptation*.

In the present study, we will assess the capacity in domain adaptation for the SEML algorithm and the ML-ωPBE functional from closed-shell organic semiconducting molecules to doublet-spin organic semiconducting radicals (Figure 1). We will achieve this goal by benchmarking its predictive power in the optimal value of ω and vertical absorption and fluorescence energies (E_{abs} and E_{fl}) between D_0 and D_1 states. We will show that organic semiconducting radicals can adopt the success of ML-ωPBE.

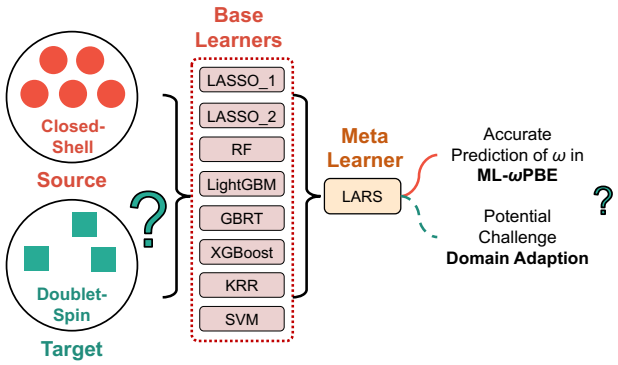

Figure 1: Architecture of the SEML model for ML-ωPBE and potential challenges in domain adaptation from closed-shell molecules to doublet-spin radicals.

Methods

Training and Test Sets

Our training set combined training and test sets from the initial development of ML-ωPBE,[84] and includes a total of 3,926 organic semiconducting molecules from six open-source and home-made datasets, including 1,941 from Harvard Clean Energy Project (CEP),[110,111] 904 from DeepChem,[112] 431 from ChemFluor,[113] 337 from Harvard Organic Photovoltaic 2015 (HOPV15),[114] 84 from uncompiled research of Aspuru-Guzik and coworkers,[115] and 229 from our compilation.[84] We also compiled a brand-new test set with 64 charge-neutral, doublet-

spin radicals. In particular, we selected 19 carbon-based radicals (C-1 through C-19),[120–133] 2 polyaromatic hydrocarbon-based radicals (PAH-20 and PAH-21),[134,135] 13 nitrogen-based radicals (N-22 through N-34),[136–144] 6 nitrogen-oxygen-based radicals (NO-35 through NO-40),[145–150] and 8 aryl oxygen-based radicals (ArO-41 through ArO-48)[151–158] to evaluate their E_{abs} values. We also selected 16 carbon-based radicals (C-49 through C-64)[17,122,127,159–165] to evaluate their E_{fl} values. We opted to use different sets of radicals for evaluating E_{abs} and E_{fl} because we wanted to reflect their most pertinent applications in electronic and biological areas as well as the availability of reliable experimental measurements. In the Supporting Information (SI), we will provide the Cartesian (XYZ) coordinates associated with optimized geometries of these radicals for D_0 and D_1 states, as well as their experimental measurements of E_{abs} or E_{fl} and optimal values of ω_{OT} and ω_{ML}. In the following sections, we will show that the absence of radical species from the training set does not undermine the predictive power of ML-ωPBE in the value of ω, electronic structures, and optical properties.

Composite Molecular Descriptor

To represent the structural and electronic configurations for all species in the training and test sets, we constructed a CMD following the same procedure as the previous study.[84] This CMD is a vector that collects information from a few computationally low-cost molecular properties, including combined molecular fingerprints (CMFs),[104–106] physical organic descriptors (PODs),[104] and semi-empirical electronic structure properties (ESPs) from tight-binding method GFN2-xTB developed by Grimme and coworkers.[107–109] Unlike closed-shell molecules in the training set, we specified the number of unpaired electrons as one for every doublet-spin radical in the test set. This tight-binding calculation turned out to be the rate-determining step for acquiring ω_{ML} from well-trained ML-ωPBE.[84]

Stacked Ensemble Machine Learning

Our "top-down" SEML algorithm, as described in detail in Figure S1 and Algorithm 1 in SI, implemented the stacked generalization of eight successful descriptor-based regression models (or *base learners*), including least absolute shrinkage and selection operator (LASSO_1 and LASSO_2, differing in molecular descriptors),[166] random forest (RF),[167] gradient boosted regression trees (GBRT),[168] eXtreme Gradient Boosting (XgBoost),[169] light gradient boosting machine (LightGBM),[170] kernel ridge regression (KRR),[171] and support vector machine (SVM).[172] We selected these regression models rather than more popular neural networks (NNs) because they are less expensive, less data-demanding, and interestingly, more potent for smaller datasets of larger organic semiconducting species.[173–180] Each base learner generated a non-linear quantitative relationship between the CMD and the optimal ω_{ML}. We also used the least angle regression (LARS)[181] method as the *meta learner* to collect and analyze the above-mentioned quantitative relationships from all base learners and provide the final prediction of ω_{ML}. Earlier studies demonstrated that stacked generalization is more powerful and accurate than every single base learner alone.[84,98–103] The source code and database associated with the present study have been uploaded to the GitHub repository of the Lin Group.[182]

Computational Details

All semi-empirical tight-binding calculations as part of CMDs were performed using GFN2-xTB developed by Grimmes and coworkers and the STO-3G minimal basis set in the xTB package,[107–109] with radical structures generated using RDKit[183] based on their simplified molecular-input line-entry systems (SMILES). All first-principles electronic structure calculations, including those using DFT, TDDFT, and complete active space self-consistent field (CASSCF), were performed using the developmental version of the Q-Chem 6.1 package.[184] Based on RDKit-generated radical structures as initial guesses, D_0 structures were optimized using ground state DFT[85,185] at the level of PBE0[70,71]/6-311+G(d), and D_1 structures were

optimized using TDDFT[186–188] at the level of CAM-B3LYP[116]/6-311+G(d). PBE0 and CAM-B3LYP were selected for geometry optimizations of D_0 and D_1, respectively, because of their proven superior performance to other functionals in earlier benchmark studies for E_{abs} and E_{fl}, respectively.[189–191] Values of ω_{OT} were optimized using the golden section search algorithm,[192] and those of ω_{ML} were generated directly using the SEML model.

Using ML-ωPBE and correct atomistic structures, optical properties E_{abs} and E_{fl} were calculated based on equations

$$E_{abs} = E(D_1|D_0) - E(D_0|D_0) \tag{3}$$

$$E_{fl} = E(D_1|D_1) - E(D_0|D_1) \tag{4}$$

These energies were compared with those generated by OT-ωPBE as well as eight conventional functionals in the assessment, including LC-ωPBE (ω = 0.200 and 0.300 a_0^{-1}),[79,80] CAM-B3LYP (ω = 0.330 a_0^{-1}),[116] ωB97X-D3 (ω = 0.250 a_0^{-1}),[74] M06-2X,[72] B3LYP,[51–53] PBE0,[70,71] and PBE.[88,89] Across all other analyses of electronic structures, 6-311+G(d) and the original version of TDDFT were used by default for all DFT-based calculations unless otherwise stated, while 6-311G(d) was employed for CASSCF calculations to reduce the memory usage. Natural orbitals (NOs) were generated from CASSCF calculations as benchmarks for DFT-calculated frontier MOs. They were obtained as eigenvectors of the CASSCF-generated one-particle density matrix ($\mathbf{P}$) and designated based on ranked occupation numbers (eigenvalues) of $\mathbf{P}$.

The switching/Gaussian implementation[193,194] of state-specific,[195–197] conductor-like polarizable continuum model (C-PCM)[198–200] was used to model the solvent effect in all DFT-based calculations. For each radical in question, the ground state version of C-PCM was employed for the geometry optimization of D_0 and the single-point calculation of E_{abs} with the slow-fast charge separation performed at the solvent-equilibrium state of D_0 (Marcus partition). In particular, the non-equilibrium perturbative scheme was adopted for E_{abs}. On the

other hand, the equilibrium excited state version of C-PCM was utilized for the geometry optimization of D_1 and the single-point calculation of E_{fl} with the slow-fast charge separation performed at the solvent-equilibrium state of D_1.[196,197,201,202] Solvents reported by corresponding experimental measurements from which our test set was compiled[17,120–143,145–164] were used in these calculations and their static and optical dielectric constants (ε_r and ε_∞) were obtained from the CRC Handbook[203] and are provided in SI.

Results

Domain Adaptation

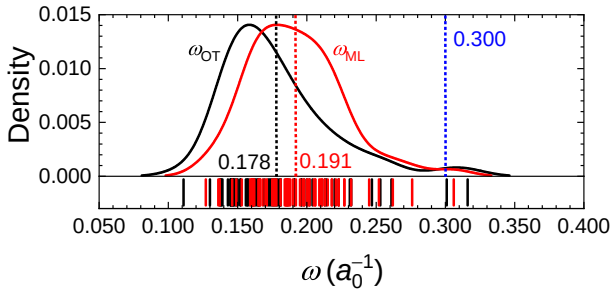

Figure 2: Distributions of ω_{ML} and ω_{OT} (a_0^{-1}) for all doublet-spin radicals from the test set, with average values $\langle\omega_{OT}\rangle = 0.178\ a_0^{-1}$ and $\langle\omega_{ML}\rangle = 0.191\ a_0^{-1}$ labeled, as well as $\omega = 0.300\ a_0^{-1}$ used in LC-ωPBE.

In the present section, we will evaluate the performance of ML-ωPBE from a few different aspects but will prioritize its potential in domain adaptation. We will confirm a high capacity of ML-ωPBE on this aspect by showing that the non-linear quantitative relationship between the CMD and ω_{ML} can be extrapolated from the domain of closed-shell organic semiconducting molecules to that of doublet-spin organic semiconducting radicals.

Figure 2 shows broad distributions of ω_{OT} and ω_{ML} between 0.120 and 0.320 a_0^{-1}, as generated for the entire test set of radicals. These lineshapes are similar to the training set,[84] and indicate the necessity to implement a molecule-dependent value of ω for any organic semiconducting radical rather than selecting a universal value if reliable electronic structures

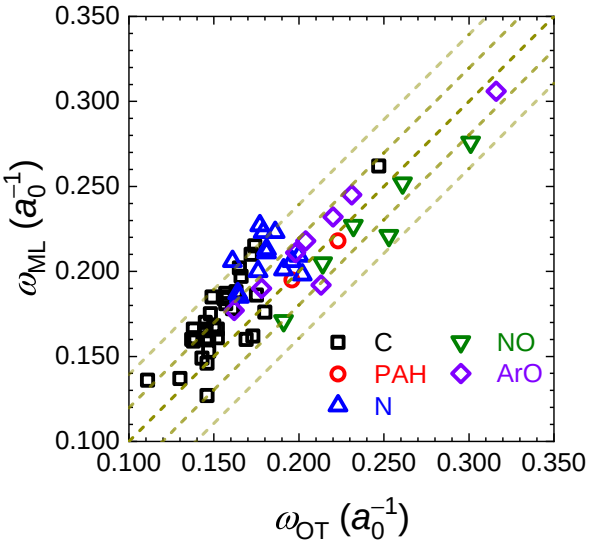

Figure 3: Comparison between ω_{ML} and ω_{OT} for all radicals from the test set, with signed errors (SEs) $\Delta\omega = \omega_{\mathrm{ML}} - \omega_{\mathrm{OT}} = 0, \pm\langle|\Delta\omega|\rangle, \pm 2\langle|\Delta\omega|\rangle$ labeled.

are needed. For example, the typical choice of $\omega = 0.300\ a_0^{-1}$ from LC-ωPBE[79] is doomed to failure to describe our radicals because the majority of ω_{ML} and ω_{OT} values are far lower than $0.300\ a_0^{-1}$. In addition, average values of $\langle\omega_{\mathrm{OT}}\rangle = 0.178\ a_0^{-1}$ and $\langle\omega_{\mathrm{ML}}\rangle = 0.191\ a_0^{-1}$ are even smaller than the training set ($\langle\omega_{\mathrm{OT}}\rangle = 0.206\ a_0^{-1}$), suggesting that doublet-spin radicals exhibit more diffusion and delocalized electronic structures in general.

Figure 3 compares ω_{ML} to ω_{OT} for all radicals from the test set and illustrates an excellent agreement. If we define the error of ω_{ML} to be the difference $\Delta\omega = \omega_{\mathrm{ML}} - \omega_{\mathrm{OT}}$, the comparison shows a small mean signed error (MSE) of $\langle\Delta\omega\rangle = 0.0139\ a_0^{-1}$ and a small MAE of $\langle|\Delta\omega|\rangle = 0.0197\ a_0^{-1}$, as well as a narrow distribution of $\Delta\omega$. We found $|\Delta\omega| < \langle|\Delta\omega|\rangle$ for 33 out of the 64 radicals and $\langle|\Delta\omega|\rangle < |\Delta\omega| < 2\langle|\Delta\omega|\rangle$ for other 27. Compared to the previous study on closed-shell molecules,[84] the MAE associated with doublet-spin radicals is more than three times as large. However, we can still claim the successful domain adaptation of ML-ωPBE because (1) this MAE value is only 11.1% of $\langle\omega_{\mathrm{OT}}\rangle$ and 10.3% of $\langle\omega_{\mathrm{ML}}\rangle$ and turns out not to significantly affect the predictive power of ML-ωPBE in further analyses of electronic structures and optical properties, and (2) there are only molecules but *no* radicals in the current training set. Regarding the computational complexity, ML-ωPBE spent an average

of 221 seconds to generate ω_{ML} for each radical, while OT-ωPBE consumed an average of 63,442 seconds to evaluate ω_{OT}, arriving at a substantial save of 99.7%. This result proves that ML-ωPBE is as successful for radicals as for molecules, with a similar capacity to generate ω to OT-ωPBE but a considerably higher efficiency.

Chemical Space

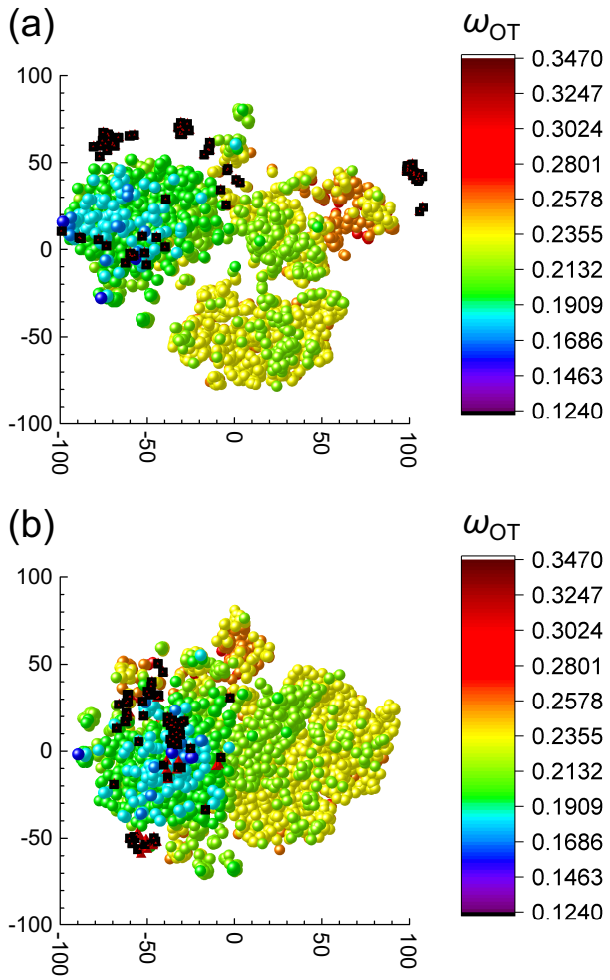

Figure 4: t-SNE results on closed-shell molecules (colorful spheres), as well as doublet-spin radicals (black cubes) along with their hydrogenated counterparts (red tetrahedrons), are described using (a) the composite ECFP4 (Morgan)[105,204] and PaDEL[205] fingerprint and (b) the simple ECFP4 fingerprint. The color bar represents the scale of ω_{OT}.

To explore the origin behind the successful domain adaptation of ML-ωPBE, we will visualize the high-dimensional CMD and analyze the chemical space occupied by training and

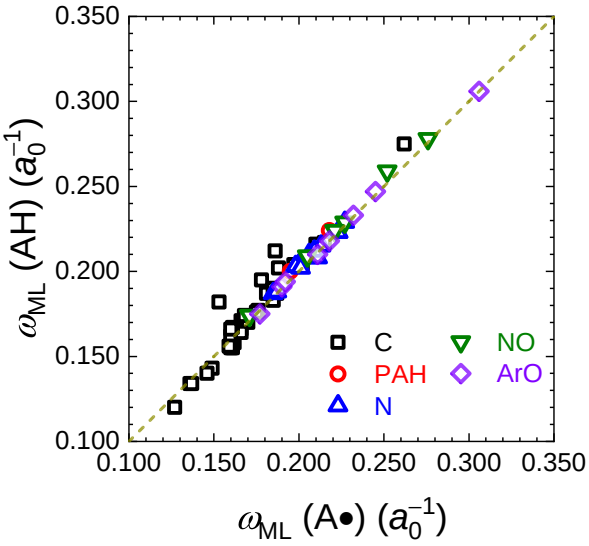

Figure 5: Comparison in ω_{ML} between all radicals from the test set and their hydrogenated counterparts.

test sets by illustrating the t-distributed stochastic neighbor embedding (t-SNE)[206] diagram with an embedded space of two (Figure 4). To extract important molecular representation features and validate the advantage of a CMD, we compared the performance of a simplified CMD constructed using ECFP4 (Morgan)[105,204] and PaDEL[205] fingerprints (Figure 4(a)), and the simple ECFP4 fingerprint (Figure 4(b)). Our t-SNE results demonstrate obviously that selected features of radicals in the test set are highly diversified as long as the chemical space is described using an appropriate CMD, and their ranges significantly overlap with molecules from the training set. This observation partially deciphers the cause of a successful domain adaptation. Also, compared to the simple ECFP4 fingerprint, the t-SNE diagram given by the simplified CMD from ECFP4 and PaDEL fingerprints shows a more substantial although not perfect natural clustering, validating a stronger capacity of CMD in differentiating species and indicating room for improvement in conventional molecular representations.[207–211]

As a further validation of the overlap in the chemical space between training and test sets, Figure 5 compares the value of ω_{ML} between every radical in the test set (A·) and its closed-shell hydrogenated counterpart (with an additional hydrogen atom attached to the

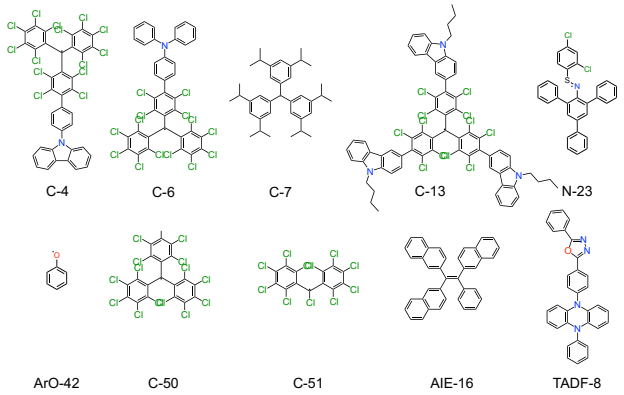

Figure 6: Structures of representative molecules from our training set and radicals from our test set.

radical site (AH) so that SOMO becomes doubly occupied). If we define their difference to be $\Delta\omega'(\mathrm{A}) = \omega_{\mathrm{ML}}(\mathrm{AH}) - \omega_{\mathrm{ML}}(\mathrm{A}\cdot)$, this comparison shows that they are very close to each other with a tiny MAE of $\langle\Delta\omega'\rangle = 0.00434\ a_0^{-1}$.

Figures S2 and S3 compare frontier α molecular orbitals (MOs) obtained from CASSCF and ML-ωPBE for two representative radicals from the test set, N-23 and C-50, as well as their hydrogenated counterparts, N-23-H and C-50-H. These two radicals show different results, allowing us to interpret our observation from Figure 5. Like most radicals, the remarkable similarity in MO configurations between N-23 and N-23-H (Figure S2) agrees with the small $\Delta\omega' = +0.002\ a_0^{-1}$ and proves that molecular features extracted by our CMD and SEML model are so robust that similar electronic structures lead to similar predictions of ω_{ML}. For a small portion of the test set, like C-50 ($\Delta\omega' = +0.029\ a_0^{-1}$, Figure S3), the large deviation is caused by a significant change in electronic structures after the additional hydrogen atom is introduced, usually a broken π-conjugation and an enhanced localization of the original SOMO. The same character shift was also reflected in CMD, especially in the tight-binding calculation.

Impact of Range Separation Parameter

Before we systematically discuss the accuracy of ML-ωPBE on radical electronic structures, we will take a short detour and examine the sensitivity of electronic structures to the choice of ω using the formula of LC-ωPBE, as motivated by the insufficient benchmark of RSH functionals on open-shell systems. To facilitate this discussion we selected two representative molecules from the training set, including AIE-16 with a locally excited (LE) singlet first excited state (S_1)[84,117] and TADF-8 with a charge transfer (CT) S_1 state,[84,119] as well as three representative radicals from the test set, including C-6 with a primarily CT D_1 state, C-7 with a primarily LE D_1 state, and N-23 with a partial CT D_1 character (Figure 6).

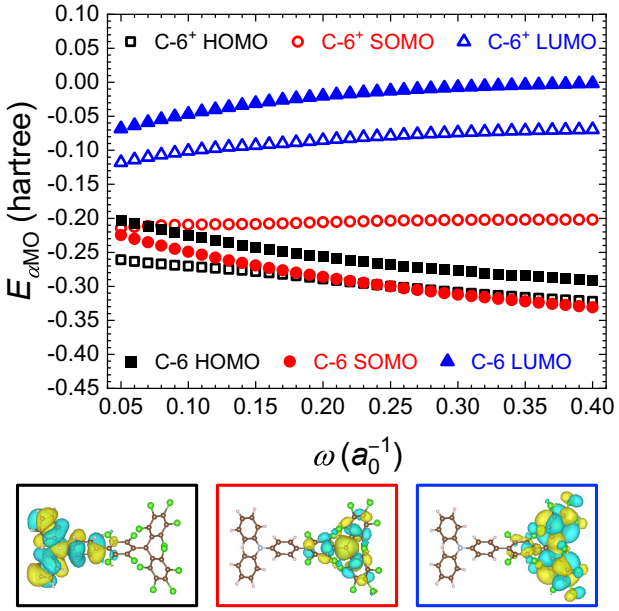

Figure 7: DFT-evaluated energies (hartree) of frontier α HOMO, SOMO, and LUMO for C-6 and C-6$^+$ as functions of ω (a_0^{-1}) at the LC-ωPBE/6-311+G(d) level.

Figures 7 and S4 illustrate configurations of frontier MOs for α electrons associated with C-6, C-7, and N-23. They were all evaluated using LC-ωPBE with various values of ω between 0.050 and 0.400 a_0^{-1}. To understand and demonstrate the change in electronic structures before and after introducing the unpaired electron to the SOMO, we also calculated orbital configurations of their corresponding closed-shell cations, namely C-6$^+$, C-7$^+$, and N-23$^+$. Figures S5 through S11 provide ω-dependent leading natural transition orbital

(NTO) pairs associated with their $D_0 \rightarrow D_1$ transitions. In addition to an expected energy decrease from an unoccupied SOMO to its occupied counterpart, C-6 also exhibits a swapped energy order between HOMO and SOMO, or, in other words, a *non-Aufbau* configuration, after involving the unpaired electron. N-23 presents a mixing between nearly degenerated HOMO−1 and HOMO. For both radicals, the β HOMO $\rightarrow$ SOMO transition dominates the $D_0 \rightarrow D_1$ transition because the corresponding energy gap is smaller than the α SOMO $\rightarrow$ LUMO transition. Limited spatial overlaps within leading NTO pairs validate their CT and partial-CT characters. C-7, on the other hand, maintains its Aufbau configuration, but its $D_0 \rightarrow D_1$ transition gives a mixture of α SOMO $\rightarrow$ LUMO and β HOMO $\rightarrow$ SOMO because of similar energy gaps. Significant spatial overlap within each of the NTO pairs confirms its LE character. These results endorse the possibility of vital change in an orbital configuration when its occupation number varies.

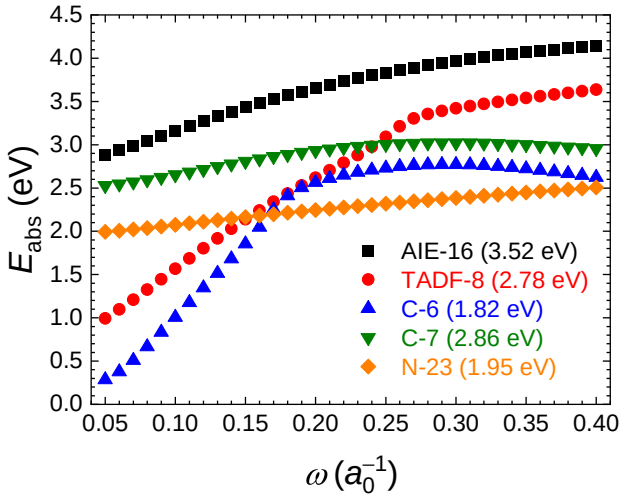

Figure 8: TDDFT-evaluated values of E_{abs} (eV) as functions of ω (a_0^{-1}) at the LC-ωPBE/6-311G+(d) level with experimental values in parentheses.

Figure 8 exhibits TDDFT-evaluated values of E_{abs} as functions of ω for AIE-16, TADF-8, C-6, C-7, and N-23, and presents bimodal trends. For AIE-16, TADF-8, and N-23, E_{abs} monotonically increases with ω as expected, because the raised effective fraction of HF exchange over-localizes electrons and over-estimates E_{abs}.[212] Their leading NTO pairs (Figures S5, S6, and S11) remain similar across the broad range of ω, except that the amplitude of CT-

transition monotonically decreases with ω, and small contributions (probability < 0.05) from other transitions may appear. On the contrary, C-6 and C-7 demonstrate non-monotonic trends in E_{abs}. Their values of E_{abs} increase first with ω, peak at $\omega = 0.310$ and 0.290 a_0^{-1}, respectively, and decrease afterward. In addition to the ever-increasing localization of MOs, their NTO pairs (Figures S7 through S10) also shift to more mixed characters, starting between 0.200 and 0.300 a_0^{-1}.

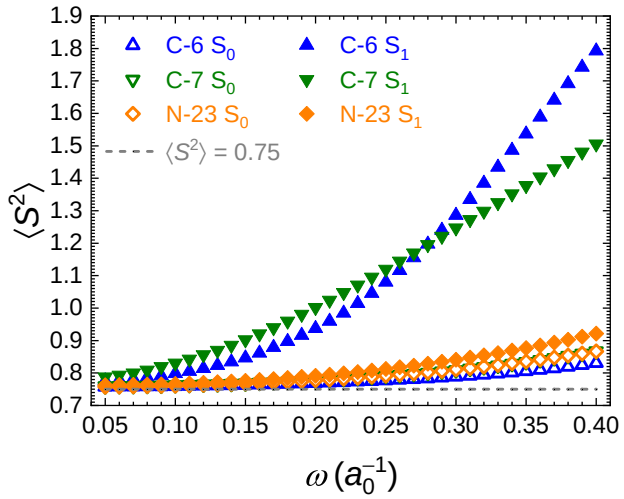

Figure 9: DFT- and TDDFT-evaluated values of $\langle S^2 \rangle$ associated with D_0 and D_1 as functions of ω (a_0^{-1}) at the LC-ωPBE/6-311+G(d) level, with $\langle S^2 \rangle = 0.75$ labeled for a pure doublet state.

Figure 9 presents total spin configurations ($\langle S^2 \rangle$) associated with D_0 and D_1 states for C-6, C-7, and N-23, and further rationalizes the mixing of NTOs. Although all radicals in question present a universally increasing spin symmetry breakdown with an increasing fraction of HF exchange, N-23 experiences no obvious shift from an expected pure doublet ($\langle S^2 \rangle = 0.75$) in both D_0 and D_1, while D_1 states of C-6 and C-7 experience more substantial mixing from quartets ($\langle S^2 \rangle = 3.75$) or even higher spin states compared to D_0. This notable breakdown of excited state spin symmetry in C-6 and C-7 agrees with the ever-increasing mixing character of NTO pairs and explains bimodal configurations for E_{abs}. The situation is exceptionally serious for C-6 because its NTO pairs are more delocalized and CT-like.

All discussions herein and later reveal an important reason for optimizing ω for organic

semiconducting radicals: intrinsic difficulty and instability embedded in RSH functionals when applied to open-shell systems, making the delicate balance between over-delocalizing PBE and over-localizing HF a key to success. In particular, excited-state electronic structures of doublet-spin radicals are susceptible to the choice of ω, especially when they exhibit more delocalized or CT characters.

Optical Band Gaps

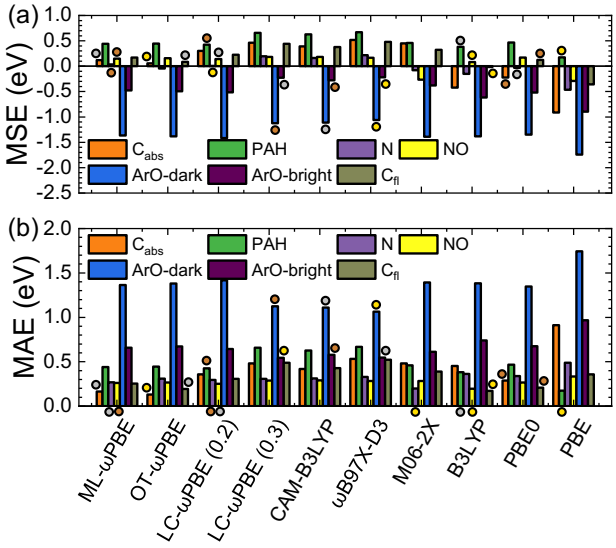

Figure 10: TDDFT-evaluated values of (a) MSEs (eV) and (b) MAEs (eV) of E_{abs} and E_{fl} at the ML-ωPBE/6-311+G(d) level for different categories of doublet-spin radicals from the test set, in comparison with nine conventional XC functionals. Functionals demonstrating the best performance and the second and third positions are labeled using gold, silver, and bronze circles.

We will benchmark ML-ωPBE by examining its predictive power of E_{abs} and E_{fl} for relevant doublet-spin radicals in the test set in the framework of TDDFT. We calibrated the precision and accuracy of ML-ωPBE-generated E_{abs} and E_{fl} in terms of their MSEs and MAEs concerning experimental measurements, and compared these results with OT-ωPBE[83,84] and eight other popular XC functionals as described in Computational Details.[51–53,70–72,74,79,80,88,89,116] We will provide statistics of MSEs and MAEs evaluated by TDDFT/6-311+G(d) in Figures 10 and 11 and Tables S1, S2, S9, and S10 in SI, and their counterparts from TDDFT/TDA/6-

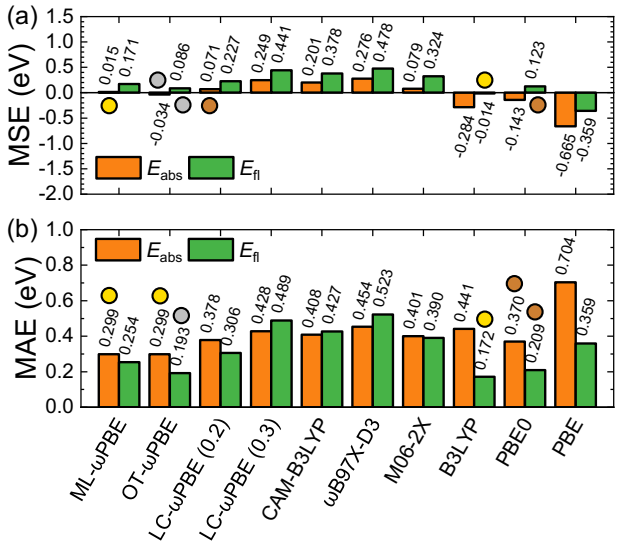

Figure 11: TDDFT-evaluated values of (a) MSEs (eV) and (b) MAEs (eV) of E_{abs} and E_{fl} at the ML-ωPBE/6-311+G(d) level for all relevant doublet-spin radicals from the test set, in comparison with nine conventional XC functionals. Functionals that demonstrate the best performance and the second and third positions are labeled using gold, silver, and bronze circles.

311+G(d), TDDFT/6-311G(d), and TDDFT/TDA/6-311G(d) in Table S3 through S10. From these results, we will draw a few conclusions about the outstanding performance of ML-ωPBE.

To begin with, we will re-validate the above-mentioned high sensitivity of the accuracy of E_{abs} and E_{fl} to the choice of ω, especially for radicals with CT D_1 states like C-6. As expected earlier, the standard LC-ωPBE functional with $\omega = 0.300\ a_0^{-1}$ shows a poor performance for almost all categories of radicals regardless of the choice of the TDDFT variant and the basis set, because $0.300\ a_0^{-1}$ is significantly larger than ω_{ML} for all radicals except for the smallest ArO-42 (Figure 6). On the other hand, Reducing ω to $0.200\ a_0^{-1}$, a value closer to $\langle\omega_{\text{OT}}\rangle = 0.178\ a_0^{-1}$ and $\langle\omega_{\text{ML}}\rangle = 0.191\ a_0^{-1}$, allows LC-$\omega$PBE to improve its performance, but it does not reach consistently comparable MAEs and MSEs with ML-ωPBE and OT-ωPBE because a fixed value of ω does not describe electronic structures for all radicals equally well. This situation becomes serious for any large π-conjugated C-based radical with a low value of ω, such as C-6 ($\omega_{\text{ML}} = 0.160\ a_0^{-1}$) for which LC-$\omega$PBE calculated values of E_{abs}

give errors of +0.741 and +0.946 eV from $\omega = 0.200\ a_0^{-1}$ and $0.300\ a_0^{-1}$, respectively. This result re-validates the necessity to apply a molecule-dependent ω to organic semiconducting radicals.

Next, we will show that well-trained ML-ωPBE outperforms the majority of conventional functionals and accurately reproduces experimental optical band gaps. Within the E_{abs} test subset, ML-ωPBE achieves the second position for C-based radicals and the third for N- and NO-based radicals (Figure 10). It also illustrates the overall top performance among all functionals with the smallest total MSE of +0.015 eV and the smallest total MAE of 0.299 eV (Figure 11). This result is only marginally different from OT-ωPBE (−0.034 and 0.299 eV). Other popular functionals like B3LYP or ωB97X-D3 occasionally perform better for some categories of radicals, but they never show a universal balance in accuracy (MAE) and precision (MSE). We attribute the success of ML-ωPBE to the excellent agreement between ω_{ML} and ω_{OT} (Figure 3), as well as the delicate balance between PBE and HF and between LE and CT. Further, this result re-affirms the robustness of ML-ωPBE among distinct domains of chemical species. In particular, our CMD can precisely represent features of these radicals, and our SEML algorithm can reliably construct a quantitative relationship between the CMD and ω_{ML}.

The behavior of ML-ωPBE on the E_{fl} test subset with all C-based radicals is also fairly good. Its performance does not enter the top three positions, but presents a reasonable agreement to OT-ωPBE and outperforms all RSH functionals (LC-ωPBE with $\omega = 0.200$ and $0.300\ a_0^{-1}$, CAM-B3LYP, and ωB97X-D3) due to a greater choice of ω. Among non-RSH functionals in comparison, two GH functionals B3LYP and PBE0, with contributions from both HF and (semi-)local exchanges, universally present smaller MSEs and MAEs for E_{fl}. This behavior is probably due to the accidental error cancellation between D_0 and D_1 or between HF and the (semi-)local exchange in use, as well as the usage of ω_{ML} that was determined from ground state properties to an excited state geometry.

To visualize and strengthen our analyses about the predictive power of ML-ωPBE in

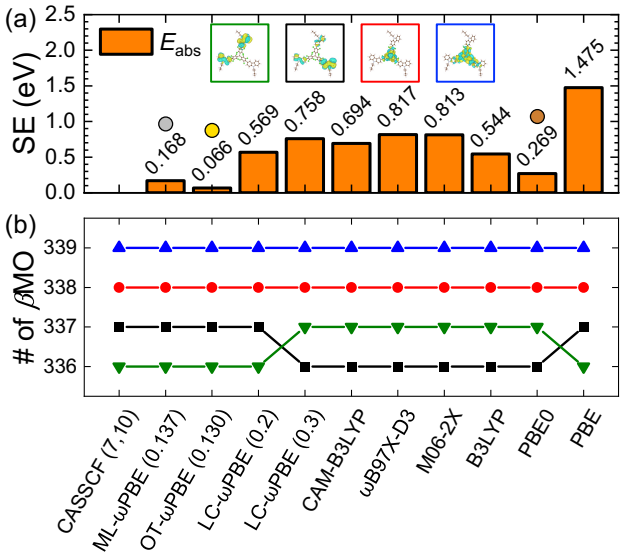

Figure 12: (a) SEs (eV) of TDDFT-evaluated E_{abs} for C-13 from various XC functionals at the 6-311+G(d) level. (b) Ordering of DFT-evaluated frontier β MOs of C-13 that bear leading characters of HOMO−1 (green), HOMO (black), SOMO (red), and LUMO (blue) from the benchmark CASSCF (7,10) calculation. Functionals that demonstrate the best performance and the second and third positions are labeled using gold, silver, and bronze circles.

radical electronic structures, we will assess the quality of frontier MOs using C-4 and C-13 as examples. Figure 12(a) gives signed errors (SEs) of E_{abs} for C-13 obtained from ML-ωPBE ($\omega = 0.137\ a_0^{-1}$), OT-ωPBE ($\omega = 0.130\ a_0^{-1}$), and all other functionals in question, and shows that errors of ML-ωPBE and OT-ωPBE are significantly smaller than other functionals. It also presents frontier β NOs for C-13 generated by the benchmark CASSCF (7,10) calculation and designated as HOMO−1, HOMO, SOMO, and LUMO based on their occupation numbers 1.9955, 1.9954, and 1.0000, and 0.0047. We found that HOMO−1 and HOMO are linear superpositions from the same set of three π orbitals but exhibit opposite symmetries. From each independent DFT calculation, we identified frontier β MOs that are involved in the $D_0 \rightarrow D_1$ transition and bear the most similar characters to NOs predicted by CASSCF (7,10), and ordered them based on energies (Figure 12(b)). We found that ML-ωPBE, OT-ωPBE, LC-ωPBE ($\omega = 0.200\ a_0^{-1}$), and PBE reproduce the order of NOs predicted by CASSCF (7,10) so that their $D_0 \rightarrow D_1$ transitions exhibit the same character. At the same time all other functionals swap HOMO−1 and HOMO and present a different

character for the same transition. In addition, considering re-ordered frontier MOs reported by PBE0 (Figure 12(b), we concluded that an excellent energy agreement with experiments does not necessarily equal a great description of electronic structures. This result justifies the importance of obtaining correct key electronic structures in predicting optical properties, and can be re-affirmed by the character of frontier α MOs from C-4 (Figure S12).

Aryl Oxygen Radicals

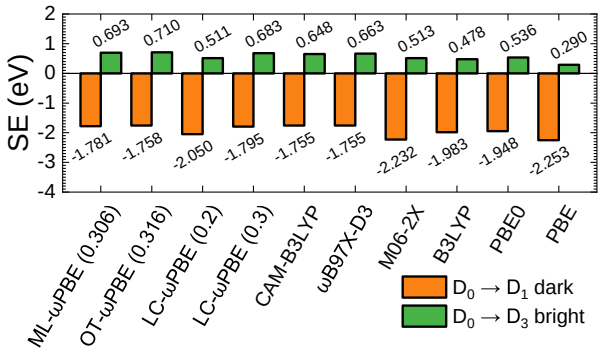

Figure 13: TDDFT-evaluated values of SEs (eV) of E_{abs} of ArO-42 for both the fundamental $D_0 \rightarrow D_1$ transition and lowest-lying bright $D_0 \rightarrow D_3$ transitions, at the ML-ωPBE/6-311+G(d) level and in comparison with nine conventional XC functionals.

We observed that DFT underestimates the value of E_{abs} by more than 1.07 eV on average for ArO-based radicals from the test set regardless of the choice of the functional, and ML-ωPBE and OT-ωPBE do not demonstrate any improvement. We will show that these vast errors originate from the existence of optically inaccessible dark D_1 states. A careful examination of all frontier MOs and dimensionless oscillator strengths

$$f_{\text{if}} = \frac{2m_e}{3\hbar^2}(E_{\text{f}} - E_{\text{i}})|\left\langle \psi_{\text{f}}|\vec{R}|\psi_{\text{i}}\right\rangle|^2 \tag{5}$$

for ArO-based radicals revealed that the lowest-lying D_1 state is typically dark due to a strong CT character and a higher symmetry. Instead, the lowest optically "bright" state with $f \geq 0.01$ appears to be D_2 for ArO-43, ArO-44, ArO-45, and ArO-46 and D_3 for ArO-41, ArO-42, and ArO-47. This observation agrees with earlier theoretical and experimental

studies of the phenoxy (ArO-42) radical.[213–215]

We re-analyzed the statistics of E_{abs} from these bright $D_0 \rightarrow D_n$ transitions, labeled them as ArO-bright in Figure 10 and Tables S1 through S8, and compared them to $D_0 \rightarrow D_1$ transitions labeled as ArO-dark. Figure 13 showcases a straightforward comparison between these two types of transitions for ArO-42. TDDFT-evaluated values of E_{abs} for these lowest bright transitions illustrate considerable enhancement in precision and accuracy compared with experimental measurement. For example, at the ML-ωPBE/TDDFT/6-311+G(d) level, MAE and MSE for ArO-based radicals are reduced from -1.378 and 1.378 eV to -0.458 and 0.651 eV, respectively. Therefore, we used ArO-bright results in overall MSEs and MAEs reported in Figure 11 and Tables S1 through S8 in place of ArO-dark.

Conclusion

In the present study, we performed a follow-up assessment of the capacity of ML-ωPBE[84] that was self-developed based on the top-down SEML strategy,[98–103] and expanded its application domain from closed-shell organic semiconducting molecules[110–115] to doublet-spin organic semiconducting radicals[17,120–165] in the framework of single-reference DFT and TDDFT. Even with only closed-shell molecules in the training set, ML-ωPBE reproduces molecule-dependent values of ω generated by OT-ωPBE with a MAE of 0.0197 a_0^{-1} over all doublet-spin radicals in the test set, but reduces the average computational cost by 2.46 orders of magnitude.

Due to capturing accurate electronic structures, ML-ωPBE demonstrates the top predictive power in experimentally observable E_{abs} for all radicals in the test set compared with popular XC functionals. It also stands among those with the best behavior for E_{fl} without prominent error cancellations. Its overall performance is only marginally different from OT-ωPBE, where it was trained from.[51–53,70–72,74,79,88,89,116] For an ArO-based radical, we found that the disagreement between the ML-ωPBE-predicted E_{abs} and the experimental

optical gap should be attributed to its dark D_1 state, and we obtained a substantially improved alignment from ML-ωPBE when its lowest-lying bright D_n state rather than D_0 was collected for E_{abs}.

In summary, through our study, we strengthened the practical value of ML-ωPBE in deciphering and predicting optical properties for luminescent organic semiconducting radicals and endorsed its potential in application in large-scale computationally aided materials discovery for various emergent areas.

Acknowledgement

Y.S., E.F., and Z.L. thank the financial support from the NSF-UMass ADVANCE Collaborative Research Seed Grant. J.Y., H.B., and Z.L. thank the financial support from UMass Amherst Start-Up Fund. All authors thank high-performance computing (HPC) resources from the UMass/URI Unity Cluster and MIT SuperCloud[216] at Massachusetts Green High Performance Computing Center (MGHPCC). All authors also thank Prof. Hui Guan, Dr. Kun Yao, Dr. Lixue (Sherry) Cheng, Dr. Xin Chen, and Mr. Junjie Yang for helpful discussions.

Supporting Information Available

The Supporting Information is available free of charge at XXXXXXXXX.

- Brief revisit of the SEML model; error statistics of ML-ωPBE and other XC functionals in optical properties; and configurations of frontier MOs and NTOs (PDF).
- Optimized D_0 geometries for 48 radicals in the test subset of E_{abs}; and optimized D_1 geometries for 16 radicals in the test subset of E_{fl} (ZIP).
- SMILES strings, experimental measurements and TDDFT calculations for E_{abs} and E_{fl}, values of ω_{OT} and ω_{ML}, and static and optical dielectric constants for all 64 radicals in

the external test set (XLSX).

References

(1) Gryn'ova, G.; Marshall, D. L.; Blanksby, S. J.; Coote, M. L. Switching Radical Stability by pH-Induced Orbital Conversion. *Nat. Chem.* **2013**, *5*, 474–481.

(2) Kumar, A.; Sevilla, M. D. SOMO–HOMO Level Inversion in Biologically Important Radicals. *J. Phys. Chem. B* **2018**, *122*, 98–105.

(3) Reineke, S. Radically More Stable. *Nat. Mater.* **2019**, *18*, 917–918.

(4) Guo, H.; Peng, Q.; Chen, X.-K.; Gu, Q.; Dong, S.; Evans, E. W.; Gillett, A. J.; Ai, X.; Zhang, M.; Credgington, D. et al. High Stability and Luminescence Efficiency in Donor–Acceptor Neutral Radicals not Following the Aufbau Principle. *Nat. Mater.* **2019**, *18*, 977–984.

(5) Tanushi, A.; Kimura, S.; Kusamoto, T.; Tominaga, M.; Kitagawa, Y.; Nakano, M.; Nishihara, H. NIR Emission and Acid-Induced Intramolecular Electron Transfer Derived from a SOMO–HOMO Converted Non-Aufbau Electronic Structure. *J. Phys. Chem. C* **2019**, *123*, 4417–4423.

(6) Cho, E.; Coropceanu, V.; Brédas, J.-L. Organic Neutral Radical Emitters: Impact of Chemical Substitution and Electronic-State Hybridization on the Luminescence Properties. *J. Am. Chem. Soc.* **2020**, *142*, 17782–17786.

(7) Abdurahman, A.; Hele, T. J. H.; Gu, Q.; Zhang, J.; Peng, Q.; Zhang, M.; Friend, R. H.; Li, F.; Evans, E. W. Understanding the Luminescent Nature of Organic Radicals for Efficient Doublet Emitters and Pure-Red Light-Emitting Diodes. *Nat. Mater.* **2020**, *19*, 1224–1229.

(8) Abella, L.; Crassous, J.; Favereau, L.; Autschbach, J. Why is the Energy of the Singly Occupied Orbital in Some Radicals below the Highest Occupied Orbital Energy? *Chem. Mater.* **2021**, *33*, 3678–3691.

(9) Kasemthaveechok, S.; Abella, L.; Crassous, J.; Autschbach, J.; Favereau, L. Organic Radicals With Inversion of SOMO and HOMO Energies and Potential Applications in Optoelectronics. *Chem. Sci.* **2022**, *13*, 9833–9847.

(10) Miller, J. S. Organic- and Molecule-Based Magnets. *Mater. Today* **2014**, *17*, 224–235.

(11) Jiao, Y.; Liu, K.; Wang, G.; Wang, Y.; Zhang, X. Supramolecular Free Radicals: Near-Infrared Organic Materials with Enhanced Photothermal Conversion. *Chem. Sci.* **2015**, *6*, 3975–3980.

(12) Jung, H. S.; Verwilst, P.; Sharma, A.; Shin, J.; Sessler, J. L.; Kim, J. S. Organic Molecule-Based Photothermal Agents: An Expanding Photothermal Therapy Universe. *Chem. Soc. Rev.* **2018**, *47*, 2280–2297.

(13) Yang, Y.; He, P.; Wang, Y.; Bai, H.; Wang, S.; Xu, J.-F.; Zhang, X. Supramolecular Radical Anions Triggered by Bacteria *In-Situ* for Selective Photothermal Therapy. *Angew. Chem. Int. Ed.* **2017**, *56*, 16239–16242.

(14) Xia, R.; Zheng, X.; Hu, X.; Liu, S.; Xie, Z. Photothermal-Controlled Generation of Alkyl Radical from Organic Nanoparticles for Tumor Treatment. *ACS Appl. Mater. Interfaces* **2019**, *11*, 5782–5790.

(15) Tang, B.; Li, W.-L.; Chang, Y.; Yuan, B.; Wu, Y.; Zhang, M.-T.; Xu, J.-F.; Li, J.; Zhang, X. A Supramolecular Radical Dimer: High-Efficiency NIR-II Photothermal Conversion and Therapy. *Angew. Chem. Int. Ed.* **2019**, *58*, 15526–15531.

(16) Peng, Q.; Obolda, A.; Zhang, M.; Li, F. Organic Light-Emitting Diodes Using a

Neutral π-Radical as Emitter: The Emission from a Doublet. *Angew. Chem. Int. Ed.* **2015**, *54*, 7091–7095.

(17) Ai, X.; Evans, E. W.; Dong, S.; Gillett, A. J.; Guo, H.; Chen, Y.; Hele, T. J. H.; Friend, R. H.; Li, F. Efficient Radical-Based Light-Emitting Diodes with Doublet Emission. *Nature* **2018**, *563*, 536–540.

(18) Hudson, J. M.; Hele, T. J. H.; Evans, E. W. Efficient Light-Emitting Diodes from Organic Radicals with Doublet Emission. *J. Appl. Phys.* **2021**, *129*, 180901.

(19) Slater, J. C. The Theory of Complex Spectra. *Phys. Rev.* **1929**, *34*, 1293–1322.

(20) Gräfenstein, J.; Cremer, D. The combination of density functional theory with multi-configuration methods – CAS-DFT. *Chem. Phys. Lett.* **2000**, *316*, 569–577.

(21) Takeda, R.; Yamanaka, S.; Yamaguchi, K. CAS-DFT based on odd-electron density and radical density. *Chem. Phys. Lett.* **2002**, *366*, 321–328.

(22) Gräfenstein, J.; Cremer, D. Development of a CAS-DFT method covering non-dynamical and dynamical electron correlation in a balanced way. *Mol. Phys.* **2005**, *103*, 279–308.

(23) Li Manni, G.; Carlson, R. K.; Luo, S.; Ma, D.; Olsen, J.; Truhlar, D. G.; Gagliardi, L. Multiconfiguration Pair-Density Functional Theory. *J. Chem. Theory Comput.* **2014**, *10*, 3669–3680.

(24) Gagliardi, L.; Truhlar, D. G.; Li Manni, G.; Carlson, R. K.; Hoyer, C. E.; Bao, J. L. Multiconfiguration Pair-Density Functional Theory: A New Way To Treat Strongly Correlated Systems. *Acc. Chem. Res.* **2017**, *50*, 66–73.

(25) Meitei, O. R.; Mayhall, N. J. Spin-Flip Pair-Density Functional Theory: A Practical Approach To Treat Static and Dynamical Correlations in Large Molecules. *J. Chem. Theory Comput.* **2021**, *17*, 2906–2916.

(26) Fromager, E.; Toulouse, J.; Jensen, H. J. A. On the universality of the long-/short-range separation in multiconfigurational density-functional theory. *J. Chem. Phys.* **2007**, *126*, 074111.

(27) Fromager, E.; Knecht, S.; Jensen, H. J. A. Multi-configuration time-dependent density-functional theory based on range separation. *J. Chem. Phys.* **2013**, *138*, 084101.

(28) Hedegård, E. D.; Toulouse, J.; Jensen, H. J. A. Multiconfigurational short-range density-functional theory for open-shell systems. *J. Chem. Phys.* **2018**, *148*, 214103.

(29) Cembran, A.; Song, L.; Mo, Y.; Gao, J. Block-Localized Density Functional Theory (BLDFT), Diabatic Coupling, and Their Use in Valence Bond Theory for Representing Reactive Potential Energy Surfaces. *J. Chem. Theory Comput.* **2009**, *5*, 2702–2716.

(30) Zhao, R.; Hettich, C. P.; Chen, X.; Gao, J. Minimal-active-space multistate density functional theory for excitation energy involving local and charge transfer states. *npj Comput. Mater.* **2021**, *7*, 148.

(31) Lu, Y.; Gao, J. Multistate Density Functional Theory of Excited States. *J. Phys. Chem. Lett.* **2022**, *13*, 7762–7769.

(32) Limacher, P. A.; Ayers, P. W.; Johnson, P. A.; De Baerdemacker, S.; Van Neck, D.; Bultinck, P. A New Mean-Field Method Suitable for Strongly Correlated Electrons: Computationally Facile Antisymmetric Products of Nonorthogonal Geminals. *J. Chem. Theory Comput.* **2013**, *9*, 1394–1401.

(33) Sun, Q.; Yang, J.; Chan, G. K.-L. A General Second Order Complete Active Space Self-Consistent-Field Solver for Large-Scale Systems. *Chem. Phys. Lett.* **2017**, *683*, 291–299.

(34) Mostafanejad, M.; DePrince, A. E. Combining Pair-Density Functional Theory and

Variational Two-Electron Reduced-Density Matrix Methods. *J. Chem. Theory Comput.* **2019**, *15*, 290–302.

(35) Hirata, S.; Lee, T. J.; Head-Gordon, M. Time-Dependent Density Functional Study on the Electronic Excitation Energies of Polycyclic Aromatic Hydrocarbon Radical Cations of Naphthalene, Anthracene, Pyrene, and Perylene. *J. Chem. Phys.* **1999**, *111*, 8904–8912.

(36) Tokmachev, A. M.; Boggio-Pasqua, M.; Mendive-Tapia, D.; Bearpark, M. J.; Robb, M. A. Fluorescence of the Perylene Radical Cation and an Inaccessible D_0/D_1 Conical Intersection: An MMVB, RASSCF, and TD-DFT Computational Study. *J. Chem. Phys.* **2010**, *132*, 044306.

(37) Weisman, J. L.; Lee, T. J.; Salama, F.; Head-Gordon, M. Time-dependent Density Functional Theory Calculations of Large Compact Polycyclic Aromatic Hydrocarbon Cations: Implications for the Diffuse Interstellar Bands. *Astrophys. J.* **2003**, *587*, 256–261.

(38) Malloci, G.; Mulas, G.; Cappellini, G.; Joblin, C. Time-Dependent Density Functional Study of the Electronic Spectra of Oligoacenes in the Charge States −1, 0, +1, and +2. *Chem. Phys.* **2007**, *340*, 43–58.

(39) Bauschlicher, C. W. Time-Dependent Density Functional Theory for Polycyclic Aromatic Hydrocarbon Anions: What is the Best Approach. *Chem. Phys. Lett.* **2005**, *409*, 235–239.

(40) Riffet, V.; Jacquemin, D.; Cauët, E.; Frison, G. Benchmarking DFT and TD-DFT Functionals for the Ground and Excited States of Hydrogen-Rich Peptide Radicals. *J. Chem. Theory Comput.* **2014**, *10*, 3308–3318.

(41) Tureček, F. Benchmarking Electronic Excitation Energies and Transitions in Peptide Radicals. *J. Phys, Chem. A* **2015**, *119*, 10101–10111.

(42) Li, Z.; Liu, W. Critical Assessment of TD-DFT for Excited States of Open-Shell Systems: I. Doublet–Doublet Transitions. *J. Chem. Theory Comput.* **2016**, *12*, 238–260.

(43) Li, Z.; Liu, W. Critical Assessment of Time-Dependent Density Functional Theory for Excited States of Open-Shell Systems: II. Doublet-Quartet Transitions. *J. Chem. Theory Comput.* **2016**, *12*, 2517–2527.

(44) Boggio-Pasqua, M.; Bearpark, M. J. Using Density Functional Theory Based Methods to Investigate the Photophysics of Polycyclic Aromatic Hydrocarbon Radical Cations: A Benchmark Study on Naphthalene, Pyrene and Perylene Cations. *ChemPhotoChem* **2019**, *3*, 763–769.

(45) Weisman, J. L.; Lee, T. J.; Head-Gordon, M. Electronic Spectra and Ionization Potentials of a Stable Class of Closed Shell Polycyclic Aromatic Hydrocarbon Cations. *Spectrochim. Acta A* **2001**, *57*, 931–945.

(46) Hirata, S.; Head-Gordon, M.; Szczepanski, J.; Vala, M. Time-Dependent Density Functional Study of the Electronic Excited States of Polycyclic Aromatic Hydrocarbon Radical Ions. *J. Phys. Chem. A* **2003**, *107*, 4940–4951.

(47) Chai, J.-D.; Head-Gordon, M. Systematic Optimization of Long-Range Corrected Hybrid Density Functionals. *J. Chem. Phys.* **2008**, *128*, 084106.

(48) Bera, P. P.; Head-Gordon, M.; Lee, T. J. Initiating Molecular Growth in the Interstellar Medium via Dimeric Complexes of Observed Ions and Molecules. *Astron. Astrophys.* **2011**, *535*, A74.

(49) Bera, P. P.; Head-Gordon, M.; Lee, T. J. Relative Energies, Structures, Vibrational Frequencies, and Electronic Spectra of Pyrylium Cation, an Oxygen-Containing Carbocyclic Ring Isoelectronic with Benzene, and its Isomers. *J. Chem. Phys.* **2013**, *139*, 174302.

(50) Hirata, S.; Head-Gordon, M. Time-Dependent Density Functional Theory within the Tamm–Dancoff Approximation. *Chem. Phys. Lett.* **1999**, *314*, 291–299.

(51) Becke, A. D. Density-Functional Exchange-Energy Approximation with Correct Asymptotic Behavior. *Phys. Rev. A* **1988**, *38*, 3098–3100.

(52) Lee, C.; Yang, W.; Parr, R. G. Development of the Colle–Salvetti Correlation-Energy Formula into a Functional of the Electron Density. *Phys. Rev. B* **1988**, *37*, 785–789.

(53) Becke, A. D. A New Mixing of Hartree–Fock and Local Density-Functional Theories. *J. Chem. Phys.* **1993**, *98*, 1372–1377.

(54) Dreuw, A.; Head-Gordon, M. Failure of Time-Dependent Density Functional Theory for Long-Range Charge-Transfer Excited States: the Zincbacteriochlorin–Bacteriochlorin and Bacteriochlorophyll–Spheroidene Complexes. *J. Am. Chem. Soc.* **2004**, *126*, 4007–4016.

(55) Dreuw, A.; Head-Gordon, M. Single-Eeference *Ab Initio* Methods for the Calculation of Excited States of Large Molecules. *Chem. Rev.* **2005**, *105*, 4009–4037.

(56) Wang, Y.-L.; Wu, G.-S. Improving the TDDFT Calculation of Low-Lying Excited States for Polycyclic Aromatic Hydrocarbons Using the Tamm–Dancoff Approximation. *Int. J Quantum Chem.* **2008**, *108*, 430–439.

(57) Hsu, C.-P.; Hirata, S.; Head-Gordon, M. Excitation Energies from Time-Dependent Density Functional Theory for Linear Polyene Oligomers: Butadiene to Decapentaene. *J. Phys. Chem. A* **2001**, *105*, 451–458.

(58) Bauernschmitt, R.; Ahlrichs, R. Stability Analysis for Solutions of the Closed Shell Kohn–Sham Equation. *J. Chem. Phys.* **1996**, *104*, 9047–9052.

(59) Sears, J. S.; Körzdörfer, T.; Zhang, C.-R.; Brédas, J.-L. Communication: Orbital

Instabilities and Triplet States from Time-Dependent Density Functional Theory and Long-Range Corrected Functionals. *J. Chem. Phys.* **2011**, *135*, 151103.

(60) Yamada, T.; Hirata, S. Singlet and Triplet Instability Theorems. *J. Chem. Phys.* **2015**, *143*, 114112.

(61) Malloci, G.; Joblin, C.; Mulas, G. On-Line Database of the Spectral Properties of Polycyclic Aromatic Hydrocarbons. *Chem. Phys.* **2007**, *332*, 353–359.

(62) Malloci, G.; Mulas, G.; Joblin, C. Electronic Absorption Spectra of PAHs Up to Vacuum UV – Towards a Detailed Model of Interstellar PAH Photophysics. *Astron. Astrophys.* **2004**, *426*, 105–117.

(63) Rapacioli, M.; Simon, A.; Marshall, C. C. M.; Cuny, J.; Kokkin, D.; Spiegelman, F.; Joblin, C. Cationic Methylene–Pyrene Isomers and Isomerization Pathways: Finite Temperature Theoretical Studies. *J. Phys. Chem. A* **2015**, *119*, 12845–12854.

(64) Dierksen, M.; Grimme, S. Density Functional Calculations of the Vibronic Structure of Electronic Absorption Spectra. *J. Chem. Phys.* **2004**, *120*, 3544–3554.

(65) Dierksen, M.; Grimme, S. The Vibronic Structure of Electronic Absorption Spectra of Large Molecules: A Time-Dependent Density Functional Study on the Influence of "Exact" Hartree–Fock Exchange. *J. Phys. Chem. A* **2004**, *108*, 10225–10237.

(66) Send, R.; Kühn, M.; Furche, F. Assessing Excited State Methods by Adiabatic Excitation Energies. *J. Chem. Theory Comput.* **2011**, *7*, 2376–2386.

(67) Bates, J. E.; Furche, F. Harnessing the Meta-Generalized Gradient Approximation for Time-Dependent Density Functional Theory. *J. Chem. Phys.* **2012**, *137*, 164105.

(68) Bates, J. E.; Heiche, M. C.; Liang, J.; Furche, F. Erratum: "Harnessing the Meta-Generalized Gradient Approximation for Time-Dependent Density Functional Theory" [J. Chem. Phys. 137, 164105 (2012)]. *J. Chem. Phys.* **2022**, *156*, 159902.

(69) Barnes, L.; Abdul-Al, S.; Allouche, A.-R. TDDFT Assessment of Functionals for Optical 0–0 Transitions in Small Radicals. *J. Phys. Chem. A* **2014**, *118*, 11033–11046.

(70) Perdew, J. P.; Ernzerhof, M.; Burke, K. Rationale for Mixing Exact Exchange with Density Functional Approximations. *J. Chem. Phys.* **1996**, *105*, 9982–9985.

(71) Adamo, C.; Barone, V. Toward Reliable Density Functional Methods without Adjustable Parameters: The PBE0 Model. *J. Chem. Phys.* **1999**, *110*, 6158–6170.

(72) Zhao, Y.; Truhlar, D. G. The M06 Suite of Density Functionals for Main Group Thermochemistry, Thermochemical Kinetics, Noncovalent Interactions, Excited States, and Transition Elements: Two New Functionals and Systematic Testing of Four M06-Class Functionals and 12 Other Functionals. *Theor. Chem. Acc.* **2008**, *120*, 215–241.

(73) Chai, J.-D.; Head-Gordon, M. Long-Range Corrected Hybrid Density Functionals with Damped Atom–Atom Dispersion Corrections. *Phys. Chem. Chem. Phys.* **2008**, *10*, 6615–6620.

(74) Lin, Y.-S.; Li, G.-D.; Mao, S.-P.; Chai, J.-D. Long-Range Corrected Hybrid Density Functionals with Improved Dispersion Corrections. *J. Chem. Theory Comput.* **2013**, *9*, 263–272.

(75) Mardirossian, N.; Head-Gordon, M. ωB97X-V: A 10-Parameter, Range-Separated Hybrid, Generalized Gradient Approximation Density Functional with Nonlocal Correlation, Designed by a Survival-of-the-Fittest Strategy. *Phys. Chem. Chem. Phys.* **2014**, *16*, 9904–9924.

(76) Henderson, T. M.; Janesko, B. G.; Scuseria, G. E. Generalized Gradient Approximation Model Exchange Holes for Range-Separated Hybrids. *J. Chem. Phys.* **2008**, *128*, 194105.

(77) Heyd, J.; Scuseria, G. E.; Ernzerhof, M. Hybrid Functionals Based on a Screened Coulomb Potential. *J. Chem. Phys.* **2003**, *118*, 8207–8215.

(78) Krukau, A. V.; Vydrov, O. A.; Izmaylov, A. F.; Scuseria, G. E. Influence of the Exchange Screening Parameter on the Performance of Screened Hybrid Functionals. *J. Chem. Phys.* **2006**, *125*, 224106.

(79) Rohrdanz, M. A.; Herbert, J. M. Simultaneous Benchmarking of Ground- and Excited-State Properties with Long-Range-Corrected Density Functional Theory. *J. Chem. Phys.* **2008**, *129*, 034107.

(80) Rohrdanz, M. A.; Martins, K. M.; Herbert, J. M. A Long-Range-Corrected Density Functional that Performs Well for Both Ground-State Properties and Time-Dependent Density Functional Theory Excitation Energies, Including Charge-Transfer Excited States. *J. Chem. Phys.* **2009**, *130*, 054112.

(81) Mardirossian, N.; Head-Gordon, M. ωB97M-V: A Combinatorially Optimized, Range-Separated Hybrid, *meta*-GGA Density Functional with VV10 Nonlocal Correlation. *J. Chem. Phys.* **2016**, *144*, 214110.

(82) Zhang, Y.; Xu, X.; Goddard, W. A. Doubly Hybrid Density Functional for Accurate Descriptions of Nonbond Interactions, Thermochemistry, and Thermochemical Kinetics. *Proc. Natl. Acad. Sci.* **2009**, *106*, 4963–4968.

(83) Lin, Z.; Van Voorhis, T. Triplet Tuning: A Novel Family of Non-Empirical Exchange–Correlation Functionals. *J. Chem. Theory Comput.* **2019**, *15*, 1226–1241.

(84) Ju, C.-W.; French, E. J.; Geva, N.; Kohn, A. W.; Lin, Z. Stacked Ensemble Machine Learning for Range-Separation Parameters. *J. Phys. Chem. Lett.* **2021**, *12*, 9516–9524.

(85) Kohn, W.; Sham, L. J. Self-Consistent Equations Including Exchange and Correlation Effects. *Phys. Rev.* **1965**, *140*, A1133–A1138.

(86) Tsuneda, T.; Suzumura, T.; Hirao, K. A new one-parameter progressive Colle–Salvetti-type correlation functional. *J. Chem. Phys.* **1999**, *110*, 10664–10678.

(87) Song, J.-W.; Hirosawa, T.; Tsuneda, T.; Hirao, K. Long-range corrected density functional calculations of chemical reactions: Redetermination of parameter. *J. Chem. Phys.* **2007**, *126*, 154105.

(88) Perdew, J. P.; Burke, K.; Ernzerhof, M. Generalized Gradient Approximation Made Simple. *Phys. Rev. Lett.* **1996**, *77*, 3865–3868.

(89) Perdew, J. P.; Burke, K.; Ernzerhof, M. Erratum: Generalized Gradient Approximation Made Simple. *Phys. Rev. Lett.* **1997**, *78*, 1396–1396.

(90) Vydrov, O. A.; Scuseria, G. E. Assessment of a long-range corrected hybrid functional. *J. Chem. Phys.* **2006**, *125*, 234109.

(91) Koopmans, T. Über die Zuordnung von Wellenfunktionen und Eigenwerten zu den Einzelnen Elektronen Eines Atoms. *Physica* **1934**, *1*, 104–113.

(92) Kronik, L.; Stein, T.; Refaely-Abramson, S.; Baer, R. Excitation Gaps of Finite-Sized Systems from Optimally Tuned Range-Separated Hybrid Functionals. *J. Chem. Theory Comput.* **2012**, *8*, 1515–1531.

(93) Livshits, E.; Baer, R. A Well-Tempered Density Functional Theory of Electrons in Molecules. *Phys. Chem. Chem. Phys.* **2007**, *9*, 2932–2941.

(94) Stein, T.; Kronik, L.; Baer, R. Reliable Prediction of Charge Transfer Excitations in Molecular Complexes Using Time-Dependent Density Functional Theory. *J. Am. Chem. Soc.* **2009**, *131*, 2818–2820.

(95) Stein, T.; Eisenberg, H.; Kronik, L.; Baer, R. Fundamental Gaps in Finite Systems from Eigenvalues of a Generalized Kohn–Sham Method. *Phys. Rev. Lett.* **2010**, *105*, 266802.

(96) Baer, R.; Livshits, E.; Salzner, U. Tuned Range-Separated Hybrids in Density Functional Theory. *Annu. Rev. Phys. Chem.* **2010**, *61*, 85–109.

(97) Kuritz, N.; Stein, T.; Baer, R.; Kronik, L. Charge-Transfer-Like $\pi \rightarrow \pi^*$ Excitations in Time-Dependent Density Functional Theory: A Conundrum and Its Solution. *J. Chem. Theory Comput.* **2011**, *7*, 2408–2415.

(98) Wolpert, D. H. Stacked Generalization. *Neural Netw.* **1992**, *5*, 241–259.

(99) Polikar, R. Ensemble Based Systems in Decision Making. *IEEE Circuits Syst. Mag.* **2006**, *6*, 21–45.

(100) Rokach, L. Ensemble-Based Classifiers. *Artif. Intell. Rev.* **2010**, *33*, 1–39.

(101) Opitz, D.; Maclin, R. Popular Ensemble Methods: An Empirical Study. *J. Artif. Intell. Res.* **1999**, *11*, 169–198.

(102) Coscrato, V.; de Almeida Inácio, M. H.; Izbicki, R. The NN-Stacking: Feature Weighted Linear Stacking through Neural Networks. *Neurocomputing* **2020**, *399*, 141–152.

(103) Breiman, L. Stacked Regressions. *Mach. Learn.* **1996**, *24*, 49–64.

(104) Yang, Q.; Li, Y.; Yang, J.-D.; Liu, Y.; Zhang, L.; Luo, S.; Cheng, J.-P. Holistic Prediction of the pK_a in Diverse Solvents Based on a Machine-Learning Approach. *Angew. Chem. Int. Ed.* **2020**, *59*, 19282–19291.

(105) Rogers, D.; Hahn, M. Extended-Connectivity Fingerprints. *J. Chem. Inf. Model.* **2010**, *50*, 742–754.

(106) Willighagen, E. L.; Mayfield, J. W.; Alvarsson, J.; Berg, A.; Carlsson, L.; Jeliazkova, N.; Kuhn, S.; Pluskal, T.; Rojas-Chertó, M.; Spjuth, O. et al. The Chemistry Development Kit (CDK) v2.0: Atom Typing, Depiction, Molecular Formulas, and Substructure Searching. *J. Cheminf.* **2017**, *9*, 1–19.

(107) Grimme, S.; Bannwarth, C.; Shushkov, P. A Robust and Accurate Tight-Binding Quantum Chemical Method for Structures, Vibrational Frequencies, and Noncovalent Interactions of Large Molecular Systems Parametrized for All *spd*-Block Elements ($Z = 1 - 86$). *J. Chem. Theory Comput.* **2017**, *13*, 1989–2009.

(108) Bannwarth, C.; Ehlert, S.; Grimme, S. GFN2-xTB–An Accurate and Broadly Parametrized Self-Consistent Tight-Binding Quantum Chemical Method with Multipole Electrostatics and Density-Dependent Dispersion Contributions. *J. Chem. Theory Comput.* **2019**, *15*, 1652–1671.

(109) Pracht, P.; Caldeweyher, E.; Ehlert, S.; Grimme, S. A Robust Non-Self-Consistent Tight-Binding Quantum Chemistry Method for Large Molecules. *ChemRxiv* **2019**, doi: 10.26434/chemrxiv.8326202.v1.

(110) Hachmann, J.; Olivares-Amaya, R.; Atahan-Evrenk, S.; Amador-Bedolla, C.; Sánchez-Carrera, R. S.; Gold-Parker, A.; Vogt, L.; Brockway, A. M.; Aspuru-Guzik, A. The Harvard Clean Energy Project: Large-Scale Computational Screening and Design of Organic Photovoltaics on the World Community Grid. *J. Phys. Chem. Lett.* **2011**, *2*, 2241–2251.

(111) Hachmann, J.; Olivares-Amaya, R.; Jinich, A.; Appleton, A. L.; Blood-Forsythe, M. A.; Seress, L. R.; Román-Salgado, C.; Trepte, K.; Atahan-Evrenk, S.; Er, S. et al. Lead Candidates for High-Performance Organic Photovoltaics from High-Throughput Quantum Chemistry–the Harvard Clean Energy Project. *Energy Environ. Sci.* **2014**, *7*, 698–704.

(112) Ramsundar, B.; Eastman, P.; Walters, P.; Pande, V. *Deep Learning for the Life Sciences: Applying Deep Learning to Genomics, Microscopy, Drug Discovery, and More*; O'Reilly Media, 2019.

(113) Ju, C.-W.; Bai, H.; Li, B.; Liu, R. Machine Learning Enables Highly Accurate Predic-

tions of PhotoPhysical Properties of Organic Fluorescent Materials: Emission Wavelengths and Quantum Yields. *J. Chem. Inf. Model.* **2021**, *61*, 1053–1065.

(114) Lopez, S. A.; Pyzer-Knapp, E. O.; Simm, G. N.; Lutzow, T.; Li, K.; Seress, L. R.; Hachmann, J.; Aspuru-Guzik, A. The Harvard Organic Photovoltaic Dataset. *Sci. Data* **2016**, *3*, 160086.

(115) Gómez-Bombarelli, R.; Aguilera-Iparraguirre, J.; Hirzel, T. D.; Duvenaud, D.; Maclaurin, D.; Blood-Forsythe, M. A.; Chae, H. S.; Einzinger, M.; Ha, D.-G.; Wu, T. et al. Design of Efficient Molecular Organic Light-Emitting Diodes by a High-Throughput Virtual Screening and Experimental Approach. *Nat. Mater.* **2016**, *15*, 1120–1127.

(116) Yanai, T.; Tew, D. P.; Handy, N. C. A New Hybrid Exchange–Correlation Functional Using the Coulomb-Attenuating Method (CAM-B3LYP). *Chem. Phys. Lett.* **2004**, *393*, 51–57.

(117) Gong, J.; Lam, J. W. Y.; Tang, B. Z. Benchmark and Parameter Tuning of Hybrid Functionals for Fast Calculation of Excitation Energies of AIEgens. *Phys. Chem. Chem. Phys.* **2020**, *22*, 18035–18039.

(118) Ali, A.; Rafiq, M. I.; Zhang, Z.; Cao, J.; Geng, R.; Zhou, B.; Tang, W. TD-DFT Benchmark for UV-Visible Spectra of Fused-Ring Electron Acceptors Using Global and Range-Separated Hybrids. *Phys. Chem. Chem. Phys.* **2020**, *22*, 7864–7874.

(119) Alipour, M.; Safari, Z. Photophysics of OLED Materials with Emitters Exhibiting Thermally Activated Delayed Fluorescence and Used in Hole/Electron Transporting Layer from Optimally Tuned Range-Separated Density Functional Theory. *J. Phys. Chem. C* **2018**, *123*, 746–761.

(120) Bejarano, F.; Olavarria-Contreras, I. J.; Droghetti, A.; Rungger, I.; Rudnev, A.; Gutiérrez, D.; Mas-Torrent, M.; Veciana, J.; van der Zant, H. S. J.; Rovira, C. et al.

Robust Organic Radical Molecular Junctions Using Acetylene Terminated Groups for C−Au Bond Formation. *J. Am. Chem. Soc.* **2018**, *140*, 1691–1696.

(121) Hattori, Y.; Kusamoto, T.; Sato, T.; Nishihara, H. Synergistic Luminescence Enhancement of a Pyridyl-Substituted Triarylmethyl Radical Based on Fluorine Substitution and Coordination to Gold. *Chem. Commun.* **2016**, *52*, 13393–13396.

(122) Ai, X.; Chen, Y.; Feng, Y.; Li, F. A Stable Room-Temperature Luminescent Biphenylmethyl Radical. *Angew. Chem. Int. Ed.* **2018**, *57*, 2869–2873.

(123) Dong, S.; Xu, W.; Guo, H.; Yan, W.; Zhang, M.; Li, F. Effects of Substituents on Luminescent Efficiency of Stable Triaryl Methyl Radicals. *Phys. Chem. Chem. Phys.* **2018**, *20*, 18657–18662.

(124) Rösel, S.; Becker, J.; Allen, W. D.; Schreiner, P. R. Probing the Delicate Balance between Pauli Repulsion and London Dispersion with Triphenylmethyl Derivatives. *J. Am. Chem. Soc.* **2018**, *140*, 14421–14432.

(125) Fischer, H.; Baer, R.; Hany, R.; Verhoolen, I.; Walbiner, M. 2,2-Dimethoxy-2-Phenylacetophenone: Photochemistry and Free Radical Photofragmentation. *J. Chem. Soc., Perkin Trans. 2* **1990**, 787–798.

(126) López, M.; Velasco, D.; López-Calahorra, F.; Juliá, L. Light-Emitting Persistent Radicals for Efficient Sensor Devices of Solvent Polarity. *Tetrahedron Lett.* **2008**, *49*, 5196–5199.

(127) Gao, Y.; Xu, W.; Ma, H.; Obolda, A.; Yan, W.; Dong, S.; Zhang, M.; Li, F. Novel Luminescent Benzimidazole-Substituent Tris(2,4,6-Trichlorophenyl)Methyl Radicals: Photophysics, Stability, and Highly Efficient Red-Orange Electroluminescence. *Chem. Mater.* **2017**, *29*, 6733–6739.

(128) Wu, X.; Kim, J. O.; Medina, S.; Ramírez, F. J.; Mayorga Burrezo, P.; Wu, S.; Lim, Z. L.; Lambert, C.; Casado, J.; Kim, D. et al. Push–Pull-Type Polychlorotriphenylmethyl Radicals: New Two-Photon Absorbers and Dyes for Generation of Photo-Charges. *Chem. Eur. J.* **2017**, *23*, 7698–7702.

(129) Gu, X.; Gopalakrishna, T. Y.; Phan, H.; Ni, Y.; Herng, T. S.; Ding, J.; Wu, J. A Three-Dimensionally π-Conjugated Diradical Molecular Cage. *Angew. Chem. Int. Ed.* **2017**, *56*, 15383–15387.

(130) Heckmann, A.; Lambert, C.; Goebel, M.; Wortmann, R. Synthesis and Photophysics of a Neutral Organic Mixed-Valence Compound. *Angew. Chem. Int. Ed.* **2004**, *43*, 5851–5856.

(131) Ballester, M.; Riera, J.; Castaner, J.; Rodriguez, A.; Rovira, C.; Veciana, J. Inert Carbon Free Radicals. 3. Monofunctionalized Radicals From Perchlorotriphenylcarbenium Hexachloroantimonate. *J. Org. Chem.* **1982**, *47*, 4498–4505.

(132) Bonvoisin, J.; Launay, J.-P.; Rovira, C.; Veciana, J. Purely Organic Mixed-Valence Molecules with Nanometric Dimensions Showing Long-Range Electron Transfer. Synthesis, and Optical and EPR Studies of a Radical Anion Derived from a Bis(Triarylmethyl)Diradical. *Angew. Chem. Int. Ed.* **1994**, *33*, 2106–2109.

(133) Teruel, L.; Viadel, L.; Carilla, J.; Fajarí, L.; Brillas, E.; Sañé, J.; Rius, J.; Juliá, L. (4-Amino-2,6-Dichlorophenyl)-bis(2,4,6-Trichlorophenyl)Methyl Radical: A New Constituent of Organic Magnetic Materials. *J. Org. Chem.* **1996**, *61*, 6063–6066.

(134) Uchida, K.; Mou, Z.; Kertesz, M.; Kubo, T. Fluxional σ-Bonds of the 2,5,8-Trimethylphenalenyl Dimer: Direct Observation of the Sixfold σ-Bond Shift via a π-Dimer. *J. Am. Chem. Soc.* **2016**, *138*, 4665–4672.

(135) Small, D.; Zaitsev, V.; Jung, Y.; Rosokha, S. V.; Head-Gordon, M.; Kochi, J. K. Intermolecular π-to-π Bonding between Stacked Aromatic Dyads. Experimental and

Theoretical Binding Energies and Near-IR Optical Transitions for Phenalenyl Radical/Radical versus Radical/Cation Dimerizations. *J. Am. Chem. Soc.* **2004**, *126*, 13850–13858.

(136) Patrascu, B.; Lete, C.; Popescu, C.; Matache, M.; Paun, A.; Madalan, A.; Ionitaa, P. Synthesis and Spectral Comparison of Electronic and Molecular Properties of Some Hydrazines and Hydrazyl Free Radicals. *Arkivoc* **2020**, *2020*, 1–10.

(137) Miura, Y.; Tanaka, A.; Hirotsu, K. ESR Studies of Nitrogen-Centered Free Radicals. 40. Exceptionally Persistent Nitrogen-Centered Free Radicals. Preparation, Isolation, and Molecular Structure of N-(Arylthio)-2,4, 6-Triphenylanilino Radicals. *J. Org. Chem.* **1991**, *56*, 6638–6643.

(138) Miura, Y.; Yamamoto, A.; Katsura, Y.; Kinoshita, M.; Sato, S.; Tamura, C. ESR Studies of Nitrogen-Centered Free Radicals. 17. [(4-Nitrophenyl)Thio](2,4, 6-Tri-Tert-Butylphenyl)Aminyl: Its Preparation, Isolation, and Molecular Structure. *J. Org. Chem.* **1982**, *47*, 2618–2622.

(139) Miura, Y.; Yamamoto, A.; Katsura, Y.; Kinoshita, M. ESR Study of Persistent Thioaminyls, N-(Arylthio)-3,5-Di-Tert-Butylphenylaminyls. *J. Org. Chem.* **1980**, *45*, 3875–3880.

(140) Miura, Y.; Tomimura, T. First Isolation of *N*-Alkoxyaminyl Radicals. *Chem. Commun.* **2001**, 627–628.

(141) Fabian, J.; Decker, D.; Mayer, R. Formation and Properties of *N*-Arylthioaminyls. *Zeitschrift fur Chemie* **1988**, *28*, 325–326.

(142) Levin, P. P.; Kokrashvili, T. A.; Kuz'min, V. A. Effect of Solvent and Substituents on Electron and Hydrogen Atom Transfer in Quenching of Quinone Triplets by Secondary Aromatic Amines. *Bulletin of the Academy of Sciences of the USSR, Division of Chemical Science* **1983**, *32*, 251–257.

(143) Miura, Y.; Tomimura, T.; Teki, Y. Heterocycle-Substituted Stable Thioaminyl Radicals: Isolation, ESR Spectra, and Magnetic Properties1. *J. Org. Chem.* **2000**, *65*, 7889–7895.

(144) Ionita, G.; Căproiu, M. T.; Meghea, A.; Maior, O.; Rovinaru, M.; Ioniță, P. Synthesis Based on 9-Amino-N-Picrylcarbazyl. *Pol. J. Chem.* **1999**, *73*, 1177–1183.

(145) Symons, M. C. R.; Pena-Nuñez, A. S. Solvation of Nitroxides. *J. Chem. Soc., Faraday Trans. 1* **1985**, *81*, 2421–2435.

(146) Imino- and Bis-Imino-Pyridines With N-Ter-Butyl-N-Aminoxyl Group: Synthesis, Oxidation and Use As Ligand Towards M_2^+ (Mn, Ni, Zn) and Gd_3^+. *J. Organomet. Chem.* **2005**, *690*, 197–210.

(147) Golubev, V. A.; Sen', V. D. Mechanism of Autoreduction of Bis(4-Methoxyphenyl)-Oxoammonium Perchlorate in Aqueous Alkali. *Russ. J. Org. Chem.* **2011**, *47*, 1313–1317.

(148) Oka, H.; Tamura, T.; Miura, Y.; Teki, Y. Synthesis and Magnetic Behaviour of Poly(1,3-Phenylene)-Based Polyradical Carrying N-Tert-Butylaminoxyl Radicals. *J. Mater. Chem.* **1999**, *9*, 1227–1232.

(149) Sueishi, Y.; Yoshioka, C.; Takemoto, K.; Kotake, Y. An Optical Spectroscopic Study on Carbon–And Oxygen-Centered Free Radical Adducts Trapped by a Bi-Functional Nitrone Spin Trap. *Zeitschrift fur Physikalische Chemie* **2002**, *216*, 1353 – 1360.

(150) Sasaki, S.; Kato, K.; Yoshifuji, M. Synthesis and Redox Properties of Crowded Triarylphosphines Carrying a Nitroxide Radical and Related Compounds. *Bull. Chem. Soc. Jpn.* **2007**, *80*, 1791–1798.

(151) Kigoshi, M.; Sato, K.; Niki, E. Oxidation of Lipids Induced by Dioctadecyl Hyponitrite and Di-*t*-Butyl Hyponitrite in Organic Solution and in Aqueous Dispersions. Effects of

Reaction Medium and Size of Radicals on Efficiency of Chain Initiation. *Bull. Chem. Soc. Jpn.* **1993**, *66*, 2954–2959.

(152) Grabner, G.; Koehler, G.; Marconi, G.; Monti, S.; Venuti, E. Photophysical Properties of Methylated Phenols in Nonpolar Solvents. *J. Phys. Chem.* **1990**, *94*, 3609–3613.

(153) Modarelli, D. A.; Rossitto, F. C.; Lahti, P. M. Convenient Unimolecular Sources of Aryloxyl Radicals I – Aryloxyoxalyl Chlorides. *Tetrahedron Lett.* **1989**, *30*, 4473–4476.

(154) Ouchi, A.; Nagaoka, S.-I.; Mukai, K. Tunneling Effect in Regeneration Reaction of Vitamin E by Ubiquinol. *J. Phys. Chem. B* **2010**, *114*, 6601–6607.

(155) Roginskii, V. A.; Dubinskii, V. Z.; Miller, V. B. Dissociation of 4-Tert-Butoxy-2, 6-Di-Tertbutylphenoxyl and Antioxid Ative Activity of Phenols with Alkoky Substituents. *Bulletin of the Academy of Sciences of the USSR, Division of Chemical Science* **1981**, *30*, 2341–2344.

(156) Orio, M.; Jarjayes, O.; Baptiste, B.; Philouze, C.; Duboc, C.; Mathias, J.-L.; Benisvy, L.; Thomas, F. Geometric and Electronic Structures of Phenoxyl Radicals Hydrogen Bonded to Neutral and Cationic Partners. *Chem. Eur. J.* **2012**, *18*, 5416–5429.

(157) Rausch, R.; Schmidt, D.; Bialas, D.; Krummenacher, I.; Braunschweig, H.; Würthner, F. Stable Organic (Bi)Radicals by Delocalization of Spin Density into the Electron-Poor Chromophore Core of Isoindigo. *Chem. Eur. J.* **2018**, *24*, 3420–3424.

(158) Mitsuoka, M.; Sakamaki, D.; Fujiwara, H. Tetrathiafulvalene-Inserted Diphenoquinone: Synthesis, Structure, and Dynamic Redox Property. *Chem. Eur. J.* **2020**, *26*, 14144–14151.

(159) Neckers, D.; Rajadurai, S.; Valdes-Aguilera, O.; Zakrzewski, A.; Linden, S. Photo-

physics and Photochemistry of P-Benzoylphenyldiphenylmethyl in Solution. *Tetrahedron Lett.* **1988**, *29*, 5109–5112.

(160) Ruberu, S. R.; Fox, M. A. Photochemical Behavior of Stable Free Radicals: The Photochemistry of Perchlorodiphenylmethyl Radical. *J. Phys. Chem.* **1993**, *97*, 143–149.

(161) Peng, Q.; Obolda, A.; Zhang, M.; Li, F. Organic Light-Emitting Diodes Using a Neutral π Radical as Emitter: The Emission from a Doublet. *Angew. Chem. Int. Ed.* **2015**, *54*, 7091–7095.

(162) Cui, Z.; Ye, S.; Wang, L.; Guo, H.; Obolda, A.; Dong, S.; Chen, Y.; Ai, X.; Abdurahman, A.; Zhang, M. et al. Radical-Based Organic Light-Emitting Diodes with Maximum External Quantum Efficiency of 10.6%. *J. Phys. Chem. Lett.* **2018**, *9*, 6644–6648.

(163) Jin, Q.; Chen, S.; Sang, Y.; Guo, H.; Dong, S.; Han, J.; Chen, W.; Yang, X.; Li, F.; Duan, P. Circularly Polarized Luminescence of Achiral Open-Shell π-Radicals. *Chem. Commun.* **2019**, *55*, 6583–6586.

(164) Hattori, Y.; Kusamoto, T.; Nishihara, H. Highly Photostable Luminescent Open-Shell (3,5-Dihalo-4-Pyridyl)bis(2,4,6-Trichlorophenyl)Methyl Radicals: Significant Effects of Halogen Atoms on Their Photophysical and Photochemical Properties. *RSC Adv.* **2015**, *5*, 64802–64805.

(165) Abdurahman, A.; Chen, Y.; Ai, X.; Ablikim, O.; Gao, Y.; Dong, S.; Li, B.; Yang, B.; Zhang, M.; Li, F. A Pure Red Luminescent β-Carboline-Substituted Biphenylmethyl Radical: Photophysics, Stability and OLEDs. *J. Mater. Chem. C* **2018**, *6*, 11248–11254.

(166) Tibshirani, R. Regression Shrinkage and Selection via the Lasso. *J. R. Stat. Soc. Series B Stat. Methodol.* **1996**, *58*, 267–288.

(167) Ho, T. K. Random Decision Forests. *Proceedings of 3rd International Conference on Document Analysis and Recognition* **1995**, *1*, 278–282.

(168) Friedman, J. H. Stochastic Gradient Boosting. *Comput. Stat. Data Anal.* **2002**, *38*, 367–378.

(169) Chen, T.; Guestrin, C. XgBoost: A Scalable Tree Boosting System. *Proceedings of the 22nd ACM SIGKDD International Conference on Knowledge Discovery and Data Mining* **2016**, 785–794.

(170) Ke, G.; Meng, Q.; Finley, T.; Wang, T.; Chen, W.; Ma, W.; Ye, Q.; Liu, T.-Y. LightGBM: A Highly Efficient Gradient Boosting Decision Tree. *Adv. Neural Inf. Process. Syst.* **2017**, *30*, 3146–3154.

(171) Vovk, V. Kernel Ridge Regression. In *Empirical Inference: Festschrift in Honor of Vladimir N. Vapnik*; Schölkopf, B., Luo, Z., Vovk, V., Eds.; Springer Berlin Heidelberg: Berlin, Heidelberg, 2013; pp 105–116.

(172) Cortes, C.; Vapnik, V. Support-Vector Networks. *Mach. Learn.* **1995**, *20*, 273–297.

(173) Balabin, R. M.; Lomakina, E. I. Support Vector Machine Regression (LS-SVM)—An Alternative to Artificial Neural Networks (ANNs) for the Analysis of Quantum Chemistry Data? *Phys. Chem. Chem. Phys.* **2011**, *13*, 11710–11718.

(174) Kamath, A.; Vargas-Hern/'andez, R. A.; Krems, R. V.; Carrington, T.; Manzhos, S. Neural Networks vs Gaussian Process Regression for Representing Potential Energy Surfaces: A Comparative Study of Fit Quality and Vibrational Spectrum Accuracy. *J. Chem. Phys.* **2018**, *148*, 241702.

(175) Zhou, Y.; Wu, J.; Chen, S.; Chen, G. Toward the Exact Exchange–Correlation Potential: A Three-Dimensional Convolutional Neural Network Construct. *J. Phys. Chem. Lett.* **2019**, *10*, 7264–7269.

(176) Sun, W.; Zheng, Y.; Yang, K.; Zhang, Q.; Shah, A. A.; Wu, Z.; Sun, Y.; Feng, L.; Chen, D.; Xiao, Z. et al. Machine Learning-Assisted Molecular Design and Efficiency Prediction for High-Performance Organic Photovoltaic Materials. *Sci. Adv.* **2019**, *5*, eaay4275.

(177) Meftahi, N.; Klymenko, M.; Christofferson, A. J.; Bach, U.; Winkler, D. A.; Russo, S. P. Machine Learning Property Prediction for Organic Photovoltaic Devices. *npj Comput. Mater.* **2020**, *6*, 166.

(178) Mahmood, A.; Wang, J.-L. Machine Learning for High Performance Organic Solar Cells: Current Scenario and Future Prospects. *Energy Environ. Sci.* **2021**, *14*, 90–105.

(179) Jiang, D.; Wu, Z.; Hsieh, C.-Y.; Chen, G.; Liao, B.; Wang, Z.; Shen, C.; Cao, D.; Wu, J.; Hou, T. Could Graph Neural Networks Learn Better Molecular Representation for Drug Discovery? A Comparison Study of Descriptor-Based and Graph-Based Models. *J. Cheminformatics* **2021**, *13*, 1–23.

(180) Fabregat, R.; Fabrizio, A.; Engel, E. A.; Meyer, B.; Juraskova, V.; Ceriotti, M.; Corminboeuf, C. Local Kernel Regression and Neural Network Approaches to the Conformational Landscapes of Oligopeptides. *J. Chem. Theory Comput.* **2022**, *18*, 1467–1479.

(181) Efron, B.; Hastie, T.; Johnstone, I.; Tibshirani, R. Least Angle Regression. *Ann. Statist.* **2004**, *32*, 407–499.

(182) Ju, C.-W.; French, E. J.; Geva, N.; Kohn, A. W.; Lin, Z. Stacked Ensemble Machine Learning for Range-Separation Parameters. `https://github.com/Lin-Group-at-UMass/ML-wPBE`, 2022.

(183) Landrum, G. RDKit: Open-Source Cheminformatics Software. 2016; `https://github.com/rdkit/rdkit/releases/tag/Release_2016_09_4`.

(184) Epifanovsky, E.; Gilbert, A. T. B.; Feng, X.; Lee, J.; Mao, Y.; Mardirossian, N.; Pokhilko, P.; White, A. F.; Coons, M. P.; Dempwolff, A. L. et al. Software for the Frontiers of Quantum Chemistry: An Overview of Developments in the Q-Chem 5 Package. *J. Chem. Phys.* **2021**, *155*, 084801.

(185) Hohenberg, P.; Kohn, W. Inhomogeneous Electron Gas. *Phys. Rev.* **1964**, *136*, B864–B871.

(186) Runge, E.; Gross, E. K. U. Density-Functional Theory for Time-Dependent Systems. *Phys. Rev. Lett.* **1984**, *52*, 997–1000.

(187) Petersilka, M.; Gossmann, U. J.; Gross, E. K. U. Excitation Energies from Time-Dependent Density-Functional Theory. *Phys. Rev. Lett.* **1996**, *76*, 1212–1215.

(188) van Leeuwen, R. Causality and Symmetry in Time-Dependent Density-Functional Theory. *Phys. Rev. Lett.* **1998**, *80*, 1280–1283.

(189) Jacquemin, D.; Wathelet, V.; Perpete, E. A.; Adamo, C. Extensive TD-DFT Benchmark: Singlet-Excited States of Organic Molecules. *J. Chem. Theory Comput.* **2009**, *5*, 2420–2435.

(190) Laurent, A. D.; Jacquemin, D. TD-DFT Benchmarks: A Review. *Int. J. Quantum Chem.* **2013**, *113*, 2019–2039.

(191) Bernini, C.; Zani, L.; Calamante, M.; Reginato, G.; Mordini, A.; Taddei, M.; Basosi, R.; Sinicropi, A. Excited State Geometries and Vertical Emission Energies of Solvated Dyes for DSSC: a PCM/TD-DFT Benchmark Study. *J. Chem. Theory Comput.* **2014**, *10*, 3925–3933.

(192) Kiefer, J. Sequential Minimax Search for a Maximum. *Proc. Am. Math. Soc.* **1953**, *4*, 502–506.

(193) Lange, A. W.; Herbert, J. M. A smooth, nonsingular, and faithful discretization scheme for polarizable continuum models: The switching/Gaussian approach. *J. Chem. Phys.* **2010**, *133*, 244111.

(194) Lange, A. W.; Herbert, J. M. Symmetric versus asymmetric discretization of the integral equations in polarizable continuum solvation models. *Chem. Phys. Lett.* **2011**, *509*, 77–87.

(195) Cammi, R.; Corni, S.; Mennucci, B.; Tomasi, J. Electronic excitation energies of molecules in solution: State specific and linear response methods for nonequilibrium continuum solvation models. *J. Chem. Phys.* **2005**, *122*, 104513.

(196) Caricato, M.; Mennucci, B.; Tomasi, J.; Ingrosso, F.; Cammi, R.; Corni, S.; Scalmani, G. Formation and relaxation of excited states in solution: A new time dependent polarizable continuum model based on time dependent density functional theory. *J. Chem. Phys.* **2006**, *124*, 124520.

(197) Herbert, J. M. Dielectric continuum methods for quantum chemistry. *WIREs Comput. Mol. Sci.* **2021**, *11*, e1519.

(198) A new method for incorporating solvent effect into the classical, ab initio molecular orbital and density functional theory frameworks for arbitrary shape cavity. *Chem. Phys. Lett.* **1995**, *240*, 253–260.

(199) Cossi, M.; Barone, V.; Cammi, R.; Tomasi, J. *Ab Initio* Study of Solvated Molecules: A New Implementation of the Polarizable Continuum Model. *Chem. Phys. Lett.* **1996**, *255*, 327–335.

(200) Barone, V.; Cossi, M. Quantum Calculation of Molecular Energies and Energy Gradients in Solution by a Conductor Solvent Model. *J. Phys. Chem. A* **1998**, *102*, 1995–2001.

(201) Mewes, J.-M.; You, Z.-Q.; Wormit, M.; Kriesche, T.; Herbert, J. M.; Dreuw, A. Experimental Benchmark Data and Systematic Evaluation of Two a Posteriori, Polarizable-Continuum Corrections for Vertical Excitation Energies in Solution. *J. Phys. Chem. A* **2015**, *119*, 5446–5464.

(202) You, Z.-Q.; Mewes, J.-M.; Dreuw, A.; Herbert, J. M. Comparison of the Marcus and Pekar partitions in the context of non-equilibrium, polarizable-continuum solvation models. *J. Chem. Phys.* **2015**, *143*, 204104.

(203) Rumble, J. R. *CRC Handbook of Chemistry and Physics*; CRC Press, 2023; Vol. 104.

(204) Glem, R. C.; Bender, A.; Arnby, C. H.; Carlsson, L.; Boyer, S.; Smith, J. Circular Fingerprints: Flexible Molecular Descriptors with Applications from Physical Chemistry to ADME. *IDrugs* **2006**, *9*, 199–204.

(205) Yap, C. W. PaDEL-Descriptor: An Open Source Software to Calculate Molecular Descriptors and Fingerprints. *J. Comput. Chem.* **2011**, *32*, 1466–1474.

(206) Hinton, G. E.; Roweis, S. Stochastic Neighbor Embedding. *Advances in Neural Information Processing Systems* **2002**, *15*.

(207) Cheng, L.; Sun, J.; Miller, T. F. I. Accurate Molecular-Orbital-Based Machine Learning Energies via Unsupervised Clustering of Chemical Space. *J. Chem. Theory Comput.* **2022**, *18*, 4826–4835.

(208) Townsend, J.; Micucci, C. P.; Hymel, J. H.; Maroulas, V.; Vogiatzis, K. D. Representation of Molecular Structures with Persistent Homology for Machine Learning Applications in Chemistry. *Nat. Comm.* **2020**, *11*, 3230.

(209) Janet, J. P.; Duan, C.; Nandy, A.; Liu, F.; Kulik, H. J. Navigating Transition-Metal Chemical Space: Artificial Intelligence for First-Principles Design. *Acc. Chem. Res.* **2021**, *54*, 532–545.

(210) Janet, J. P.; Kulik, H. J. Resolving Transition Metal Chemical Space: Feature Selection for Machine Learning and Structure–Property Relationships. *J. Phys. Chem. A* **2017**, *121*, 8939–8954.

(211) Naveja, J. J.; Medina-Franco, J. L. Finding Constellations in Chemical Space Through Core Analysis. *Front. Chem.* **2019**, *7*, 510.

(212) Cohen, A. J.; Mori-Sánchez, P.; Yang, W. Challenges for Density Functional Theory. *Chem. Rev.* **2012**, *112*, 289–320.

(213) Radziszewski, J. G.; Gil, M.; Gorski, A.; Spanget-Larsen, J.; Waluk, J.; Mróz, B. J. Electronic states of the phenoxyl radical. *J. Chem. Phys.* **2001**, *115*, 9733–9738.

(214) Cheng, C.-W.; Lee, Y.-P.; Witek, H. A. Theoretical Investigation of Molecular Properties of the First Excited State of the Phenoxyl Radical. *J. Phys. Chem. A* **2008**, *112*, 2648–2657.

(215) Johnston, L. J.; Mathivanan, N.; Negri, F.; Siebrand, W.; Zerbetto, F. Assignment and vibrational analysis of the 600 nm absorption band in the phenoxyl radical and some of its derivatives. *Can. J. Chem.* **1993**, *71*, 1655–1662.

(216) Reuther, A.; Kepner, J.; Byun, C.; Samsi, S.; Arcand, W.; Bestor, D.; Bergeron, B.; Gadepally, V.; Houle, M.; Hubbell, M. et al. Interactive Supercomputing on 40,000 Cores for Machine Learning and Data Analysis. *2018 IEEE High Performance Extreme Computing Conference (HPEC)* **2018**, 1–6.

TOC Graphic